GOCI Yonsei Aerosol Retrieval (YAER) Algorithm and Validation During DRAGON-NE Asia 2012 Campaign

Myungje Choi[1], Jhoon Kim[1], Jaehwa Lee[2,3], Mijin Kim[1], Young-Je Park[4], Ukkyo Jeong[1], Woogyung Kim[1], Hyunkee Hong[5], Brent Holben[3], Thomas F. Eck[3,6], Chul Han Song[7], Jae Hyun Lim[8], Chang Keun Song[8]

[1] Department of Atmospheric Sciences, Yonsei University, Seoul, Republic of Korea

[2] Earth System Science Interdisciplinary Center, University of Maryland, College Park, MD, USA

[3] NASA Goddard Space Flight Center, Greenbelt, MD, USA

[4] Korea Ocean Satellite Center, Korea Institute of Ocean Science and Technology, Ansan, Republic of Korea

[5] Department of Spatial Information Engineering, Pukyong National University, Busan, Republic of Korea

[6] Universities Space Research Association, Columbia, MD, USA

[7] School of Environmental Science and Engineering, Gwangju Institute of Science and Technology (GIST), Gwangju, Korea

[8] National Institute of Environmental Research (NIER), Incheon, Republic of Korea

Correspondence to: Jhoon Kim (jkim2@yonsei.ac.kr)

Abstract

The Geostationary Ocean Color Imager (GOCI) onboard the Communication, Ocean, and Meteorological Satellite (COMS) is the first multi-channel ocean color imager in geostationary orbit. Hourly GOCI top-of-atmosphere radiance has been available for the retrieval of aerosol optical properties over East Asia since March 2011. This study presents improvements made to the GOCI Yonsei Aerosol Retrieval (YAER) algorithm together with validation results during the Distributed Regional Aerosol Gridded Observation Networks - North East Asia 2012 campaign (DRAGON-NE Asia 2012 campaign). The evaluation during the spring season over East Asia is important because of high aerosol concentrations and diverse types with Asian dust and haze. Optical properties of aerosol are retrieved from the GOCI YAER algorithm including aerosol optical depth (AOD) at 550 nm, fine-mode fraction (FMF) at 550 nm, single scattering albedo (SSA) at 440 nm, Angstrom exponent (AE) between 440 and 860 nm, and aerosol type. The aerosol models are created based on a global analysis of the Aerosol Robotic Networks (AERONET) inversion data, and covers broad range of size distribution and absorptivity including nonspherical dust properties. The Cox-Munk ocean bidirectional reflectance distribution function (BRDF) model is used over ocean, and improved minimum reflectance technique is used over land. Because turbid water is persistent over the Yellow Sea, the land algorithm is used for such cases. The aerosol products are evaluated against AERONET observations and MODIS Collection 6 aerosol products retrieved from "Dark Target (DT)" and "Deep Blue (DB)" algorithms during the DRAGON-NE Asia 2012 campaign conducted from March to May, 2012. Comparison of

AOD from GOCI and AERONET resulted in a Pearson correlation coefficient of 0.881 and a linear regression equation with GOCI AOD = 1.083 × AERONET AOD – 0.042. The correlation between GOCI and MODIS AODs are higher over ocean than land. GOCI AOD shows better agreement with MODIS DB than MODIS DT. The other GOCI YAER products (AE, FMF, and SSA) show lower correlation with AERONET than AOD, but still show some skills for qualitative use.

1. Introduction

Aerosols have an important role in the Earth's climate system, influencing climate directly through scattering and absorbing radiation, and indirectly by acting as cloud condensation nuclei (IPCC, 2013). Both ground-based and satellite measurements show an increasing trend of aerosol optical depth (AOD) over East Asia (IPCC, 2013; Hsu et al., 2012; Yoon et al., 2014). In particular, the increasing trend over Asia is strongest during the dry seasons from December to May. Furthermore, aerosol types over East Asia are more complex than over other regions (Kim et al., 2007a; Lee et al., 2010a). To quantify its impact on climate, accurate observation of aerosol over broad area is required.

Aerosol can be detected by remote sensing from ground-based and satellite measurement. AERONET (Aerosol Robotic Networks) is the representative global network of ground-based sun photometers, with an absolute observation uncertainty for a single AOD measurement of ±0.01 (Holben et al., 1998; Eck et al., 1999). Satellite observations from low earth orbit (LEO) and geostationary earth orbit (GEO) allow detection of aerosol properties over a wider area. Many aerosol retrieval algorithms have been developed and improved using multi-channel

sensors in LEO such as the Moderate Resolution Imaging Spectroradiometer (MODIS), Sea-Viewing Wide Field-of-View Sensor (SeaWiFS), Medium Resolution Imaging Spectrometer (MERIS), Ozone Monitoring Instrument (OMI), and Visible Infrared Imaging Radiometer Suite (VIIRS) (Higurashi and Nakajima, 1999; Kim et al., 2007a; Hsu et al., 2006; 2013; Jackson et al., 2013; Kaufman et al., 1997a; Levy et al., 2007; 2013; Remer et al., 2005; Sayer et al., 2012; Torres et al., 1998; 2007; 2012; von Hoyningen-Huene et al., 2011). Multi-channel observations from LEO give global coverage at high accuracy but with the disadvantage of low temporal resolution. The uncertainty in the retrieved AOD from MODIS is reported as ±(0.03 + 5%) over ocean and ±(0.05 + 15%) over land (Remer et al., 2008; Levy et al., 2010). Aerosol retrieval algorithms have also been developed using meteorological imagers aboard GEO satellites, such as the Geostationary Operational Environmental Satellite (GOES), Geostationary Meteorological Satellite (GMS), and Multifunction Transport Satellite (MTSAT) (Kim et al., 2008; Knapp et al., 2002; Wang et al., 2003; Yoon et al., 2007; Urm and Sohn, 2005). These sensors provide observations at a higher temporal resolution than LEO sensors, but have fixed observation area and lower accuracy due to the wider spectral bands and fewer visible channels. The magnitude of the uncertainty in the retrieved AOD using GOES has been reported as ±0.13 (Knapp et al., 2005). Despite the extensive observations to date, the confidence level of satellite-based globally averaged AOD trends is still 'low' (IPCC, 2013).

The Geostationary Ocean Color Imager (GOCI) onboard the Communication, Ocean, and Meteorological Satellites (COMS) is the first multi-channel visible– and near infrared–wavelength sensor in GEO (Ahn et al., 2012; Choi et al., 2012; Kang et al.). The wavelength bands of the eight channels are centered at 412, 443, 490, 555, 660, 680, 745 and 865 nm, similar to other ocean color sensors such as the Coastal Zone Color Scanner (CZCS),

90 SeaWiFS, MERIS, and MODIS, but GOCI has high spatial resolution of 500 m × 500 m
91 (Table 1.). It observes East Asia hourly during the daytime, a total of eight times per day. A
92 prototype of the GOCI Yonsei AErosol Retrieval (YAER) algorithm was developed (Lee et
93 al., 2010b) and is improved in this study to include dynamic (changing with AOD) and non-
94 spherical aerosol models as introduced in (Lee et al., 2012). Aerosol optical properties (AOPs)
95 such as aerosol optical depth, size information, and absorptivity can be retrieved hourly from
96 the GOCI YAER algorithm with spatial resolution of 6 km × 6 km. The high temporal
97 information on AOPs over East Asia from GOCI is expected to help understand the diurnal
98 variation of aerosol properties and improve the accuracy of air quality modeling (Park et al.,
99 2014; Saide et al., 2014; Xu et al., 2015).

100 The Distributed Regional Aerosol Gridded Observation Networks - North East Asia 2012
101 campaign (DRAGON-NE Asia 2012 campaign) took place in Korea and Japan from 1 March
102 to 31 May to observe aerosol properties and its variability using a dense network of ground-
103 based sun photometers. The campaign provides a dataset for validation of aerosol retrieval
104 algorithms in high spatial resolution.

105 This study introduces the improvements made to the GOCI YAER algorithm and validation
106 results during the DRAGON-NE Asia 2012 campaign. Because MODIS data were used for
107 the prototype algorithm before the launch of GOCI, this study is the first to use real GOCI
108 data. The GOCI YAER products are validated with AERONET data from 38 sites during the
109 DRAGON-NE Asia 2012 campaign. Inter-comparison of AOPs between GOCI and MODIS
110 Collection 6 (C6) is also performed for the same period.

111 In Section 2, the improvements of the GOCI YAER algorithm are summarized. In Section 3,
112 some aerosol event cases are analyzed using products from the improved algorithm. In

Section 4, the GOCI YAER products are validated with AERONET and MODIS. In Section 5, an error analysis of GOCI YAER AOD against AERONET AOD is presented. Section 6 provides a summary and conclusions.

2. Improvements of the GOCI YAER algorithm

Since the distribution of GOCI Level 1B (L1B) radiation data in March 2011, the GOCI YAER algorithm has been updated to process the real GOCI data and to improve the data quality. Figure 1 shows the flowchart for the GOCI YAER algorithm. The improvements made to the algorithm as compared to described in Lee et al. (2010b) will be discussed according to the sequence shown in the flowchart. The algorithm uses top-of-atmosphere (TOA) reflectance (ρ_{TOA}) as input data,

$$\rho_{TOA}(\lambda) = \frac{\pi \cdot L(\lambda)}{\mu_0 \cdot E_0(\lambda)}, \quad (1)$$

where λ is the wavelength of each GOCI channel (412, 443, 490, 555, 660, 680, 745, and 865 nm), $L(\lambda)$ is observed radiance from GOCI, μ_0 is the cosine of the solar zenith angle (θ_0), and E_0 is the extraterrestrial solar flux.

2.1 Cloud Masking and quality assurance

The algorithm is applied to cloud-free and snow-free pixels over land and cloud-free and ice-free pixels over ocean. In order to mask out the cloudy scenes, the following test are applied:

1. ρ_{TOA}(490 nm) > 0.40 → cloud over land or ocean
2. Standard deviation of 3 × 3 pixels ρ_{TOA}(412 nm) > 0.0025 → cloud over land

Standard deviation of 3 × 3 pixels ρ_{TOA}(550 nm) > 0.0025 → cloud over ocean

3. ρ_{TOA}(412 nm) / ρ_{TOA}(660 nm) > 0.75 → Dust over ocean (not masked)

The standard deviation test over land is based on the MODIS DB algorithm (Hsu et al., 2004), and other tests are based on the MODIS DT (Remer et al., 2005). Note that ocean pixels with glint angle less than 40° are also masked out. After the cloud masking, 12 × 12 GOCI 500 m resolution pixels (resulting in 6 km × 6 km resolution) are aggregated to be fed into the retrieval process. In this step, the darkest 20% and the brightest 40% of pixels in reference to ρ_{TOA}(490nm) are discarded to remove remaining cloud, cloud shadow, and surface contamination (Remer et al., 2005; Levy et al., 2007). The number of L1B pixels remaining and the retrieved AOD at 550 nm determine the quality assurance (QA) flag for each retrieval pixel, as listed in Table 2. Thresholds of QA determination are based on the MODIS DT algorithm (Levy et al., 2013). The GOCI YAER algorithm allows a retrieved AOD range to from –0.1 to 5.0, and QA can be only greater than 1 only when the value is in the range between –0.05 and 3.6. The algorithm allows randomly retrieved, small negative AOD caused by uncertainty in surface reflectance because it is within expected retrieval error as MODIS DT algorithm, and also has statistical meaning in low AOD range (Levy et al., 2007; 2013).

2.2 Surface reflectance over land and ocean

The lack of a 2.1-μm channel in GOCI limits the capability of estimating surface reflectance in the visible from the 2.1-μm TOA reflectance as in the MODIS DT algorithm (Levy et al., 2007; Kaufman et al., 1997b). Instead, the GOCI YAER algorithm uses the minimum reflectivity technique to determine the surface reflectance (ρ_{SFC}) over land and turbid water

(Herman and Celarier, 1997; Hsu et al., 2004; Koelemeijer et al., 2003). First, each scene's TOA reflectance is corrected for Rayleigh scattering to derive the Rayleigh-corrected reflectance (RCR) (Hsu et al., 2013). It is assumed that in a 30-day period, changes in surface reflectance are insignificant and there is at least one clear day (Lee et al., 2010b). To increase the number of samples to find clear pixels, it is also assumed that the surface reflectance is homogeneous over 12 × 12 pixels, so that L1B resolution data is used for determining the minimum reflectance. Thus, the spatial resolution of surface reflectance is the same as the aerosol retrieval resolution of 6 km × 6 km. To allow for changes of surface reflectance with sun–satellite geometry, RCRs at a given hour during the day are composited for each month. The maximum number of samples available to determine surface reflectance at a pixel is 144 pixels × 30 days, a total of 4,320 samples. Samples are sorted in ascending order according to RCR at 412 nm and selected from the darkest 1% to 3%. At 412 nm, the variability of surface reflectance is lower and atmospheric signals such as Rayleigh scattering or aerosol reflectance are higher than at longer wavelengths. Thus, the RCR at 412 nm is used to find clear pixels during the 30-day window. According to Hsu et al. (2004), surface reflectance database can be obtained by finding the minimum value of the 412 nm RCR within a given month, which corresponds to about 3% for the window. In this process, cloud shadows which could lead to false reflectance should not be selected to evaluate surface reflectance. For example, Lee et al. (2010b) selected the second minimum value, and Fukuda et al. (2013) used the modified minimum reflectance method using first and second minimum values to avoid cloud shadow effects for determining surface reflectance. In GOCI YAER algorithm, the maximum number of L1B pixel samples for one surface reflectance pixel at a given time is 144 pixels × 30 days, a total of 4,320 samples. Therefore, only first or second minimum threshold is not appropriate for GOCI YAER algorithm. Instead, darkest 0-1% pixels are

assumed to be cloud shadow thus excluded, empirically. Therefore, threshold for the lower and upper bound are set as 1% and 3%, respectively. The RCRs of selected pixels are averaged for each channel, giving a surface reflectance corresponding to the middle of each month (day 15). Finally, linear interpolation according to retrieval date is applied.

Figure 2 shows examples of surface reflectance at 443 and 660 nm; the difference in the surface reflectance between ocean and land is smaller at 443 nm than 660 nm. The high 660 nm surface reflectance near the coast of China in the Bohai Sea and in the northern East China Sea shows turbid water with value comparable to the land surface reflectance over northern China and higher than southern China; this clearly shows a semi-permanent presence of turbid water pixels during the 30 days. From March to May, surface reflectances decrease over land because of melting snow and increasing vegetation. According to von Hoyningen-Huene et al. (2003) which described the aerosol retrieval algorithm using ocean color sensors, pixels of which surface reflectance less than 0.15 correspond to the fully or partly covered with vegetation area. Also, Zhang et al. (2011) described that the operational GOES AOD retrieval algorithm use simple threshold of 0.15 surface reflectance to remove bright surface reflectance pixels. Final selected channels for retrieving aerosol over land are those of which surface reflectances are less than 0.15.

On the other hand, it is assumed that ocean surface reflectance varies with geometry and wind speed (Cox and Munk, 1954); the wind speed at 10 meters above sea level is used in a radiative transfer model to calculate the Look-up Table (LUT). The nodal points of wind speed in the LUT calculation are 1, 3, 5, 7, 9, and 20 m s^{-1}, which are the default nodal points of libRadtran package. Using ECMWF wind speed data with 0.25 ° × 0.25 ° spatial resolution at every 6-hour, the LUT is interpolated to each pixel's wind speed to retrieve AOD over the

ocean.

2.3 Turbid water detection

Retrieving aerosol properties over turbid water is challenging due to the variability of thee turbid water and high surface reflectance. Half of the ocean in the GOCI observation area is the Yellow Sea with very high year-round turbidity. If the ocean surface is assumed over turbid water, the surface reflectance can be underestimated, and thus AOD can be overestimated. The previous GOCI YAER algorithm (Lee et al., 2010b) used the surface reflectance ratio (SRR) for turbid water detection, which is the ratio of surface reflectance at 640 and 860 nm. If turbid water pixels are detected, the surface reflectance from the second minimum RCR during the previous 30-day period is used for AOD retrieval. Persistent–turbid areas during the previous 30 days can be detected in this way, but it is hard to detect rapid temporal variations of turbidity. In this study, real-time turbid water detection is applied.

According to Li et al. (2003), ρ_{TOA} at 550, 660, and 865 nm showed higher values over turbid water than over clear water. They used the difference between ρ_{TOA} at 550 nm and the value interpolated to 550 nm from ρ_{TOA} at 470, 1240, 1640, and 2130 nm using a linear fit on a log–log scale. In this study, because GOCI does not have IR channels, $\Delta\rho_{660}$ is defined as the difference in reflectance at 660 nm between the observed ρ_{TOA} at 660 nm and linearly interpolated between ρ_{TOA} at 412 and 865 nm to 660 nm. Increased ρ_{TOA} due to turbid water is stronger at 660 nm than at 412 and 865 nm so that $\Delta\rho_{660}$ shows a higher value over turbid water than over clear water.

To determine the threshold of $\Delta\rho_{660}$ for distinguishing turbid and clear water over the ocean, hourly data for the 1st and 15th day of each month for 3 years from March 2011 to February

223 2014 are analyzed. The analysis is implemented over two distinct areas: the Yellow Sea
224 (115°E–126°E, 30°N–40°N) and an area of clear water (130°E–140°E, 25°N–30°N), as in
225 Lee et al. (2010b). A strict threshold for defining pixels as clear water is necessary to prevent
226 misdetection of less turbid water as aerosol. Figure 3 shows the cumulative normal
227 distribution of $\Delta\rho_{660}$, where ratios below –0.05 are 99.0% and 67.4% for clear water and
228 Yellow Sea pixels, respectively. Finally, pixels with $\Delta\rho_{660}$ below –0.05 are not considered
229 as turbid water so that the ocean algorithm is applied. On the contrary, pixels where $\Delta\rho_{660}$ is
230 above –0.05 are considered as turbid water so that the land algorithm is applied. Note that the
231 surface reflectance of turbid water pixels is adjusted to the minimum turbidity during the 30
232 days so that surface reflectance can be underestimated when severely turbid water occurs
233 within the 30 days. Values of the ratio below 0.02 comprise 99.6% of the Yellow Sea pixels.
234 Therefore, pixels where $\Delta\rho_{660}$ is above 0.02 are considered as severely turbid water, and
235 excluded from the retrieval procedure.

236 To confirm whether $\Delta\rho_{660}$ effectively detects turbid water, two turbid water cases are
237 selected in Fig. 4. One is a clean atmosphere case (26 April, 2012), and another case involves
238 dust over the northern part of the Yellow Sea (27 April, 2012). To compare the sensitivity
239 between pixels over turbid water and those with absorbing aerosol, the Deep blue Aerosol
240 Index (DAI) is calculated using GOCI TOA reflectance at 412 and 443 nm (Hsu et al., 2004,
241 2006; Ciren and Kondragunta, 2014). Note that DAI and $\Delta\rho_{660}$ are plotted over cloud-free
242 pixels, and only positive DAI pixels are presented to check the existence of absorbing aerosol
243 such as dust in Fig. 4(e) and (f), because absorbing aerosol such as dust or smoke shows a
244 DAI greater than 4 over ocean (Ciren and Kondragunta, 2014). The true color image for the
245 clean case shows severe turbidity in the ocean along the coast of eastern China and the

western Korean Peninsula. The next day, there is heavy Asian dust over northern Yellow Sea, and turbid water is in the same position as the day before. $\Delta\rho_{660}$ shows a higher signal over turbid water (~0.02) than Asian dust (~–0.01), while DAI shows a higher signal over Asian dust (~4.8) than turbid water (~1.6). Although heavy aerosol plumes can have $\Delta\rho_{660}$ above –0.05 over clear water, this does not cause significant issue because the land algorithm is instead applied, not affecting spatial coverage.

An additional role of $\Delta\rho_{660}$ is to detect the remaining cloud-contaminated pixels after cloud masking. There are inhomogeneous cloud pixels over the right half of the scene in Fig. 5. Most cloud pixels are effectively screened by the cloud-masking steps, but thin cloud pixels remain and show high $\Delta\rho_{660}$ above 0.05 (red color). This is a similar to the "Visible Reflectance Anomaly" of the VIIRS aerosol algorithm (Jackson et al., 2013). Because pixels with $\Delta\rho_{660}$ above 0.02 are considered as severe turbid water and screened, the remaining cloud pixels are also masked using this test. The average ratio of pixels of $\Delta\rho_{660}$ above 0.02 after cloud masking over total available ocean pixels is about 2 % during the campaign.

2.4 Aerosol Models

There are various factors to determine aerosol characteristics and its change such as temporal and spatial variations of the direct emission, secondary production, and meteorological transport (Yoon et al., 2011; 2014; 2012). And, it is important to reflect those properties well in the aspect of optical properties for aerosol retrieval. Assumed aerosol models play an important role in the retrieval accuracy. To reflect global climatological properties, AERONET inversion data (Dubovik and King, 2000) are used for creating aerosol models to be used in the retrieval process. A classification method for AERONET inversion data using Fine-mode fraction (FMF) at 550 nm and Single scattering albedo (SSA) at 440 nm is

adopted (Kim et al., 2007a; Lee et al., 2010a; Lee et al., 2012), but there are some differences for the GOCI YAER algorithm.

Composited AERONET data are only used for the period up to February 2011, which is before GOCI's first observation, to separate AERONET data usages for aerosol model construction and validation of satellite products. Global sites are selected where the number of individual AERONET retrieval data is greater than 10 times, giving a total of 747 sites. Observation periods of individual AERONET site are quite different from few individual observations to several years. Level 2.0 data are quality assured so that each individual observation is meaningful even if whole observation period is short. Therefore, we tried to use available AERONET individual data, and small threshold of 10 times is applied. From those sites, the number of data that have all the AOPs in all channels is 66,712. They are classified into 26 aerosol models according to FMF at 550 nm and SSA at 440 nm (Table 3). Note that AOPs changes as AOD varies because of the hygroscopic growth effect or aggregation (Reid et al., 1998; Eck et al., 2003). Therefore, each aerosol model is separated again into low, moderate, and high AOD groups corresponding to the AOD ranges of 0.0–0.5, 0.5–0.8, and 0.8–3.6 respectively. Finally, the AOPs of each aerosol model are averaged and used as input for LUT calculation.

The AERONET inversion algorithm considers aerosol nonsphericity using a mixture of polydisperse, randomly-oriented homogeneous spheroids (Mishchenko et al., 1997; Dubovik et al., 2006). Phase functions of the inversion data including the effect of nonspherical particles are directly used for the radiative transfer calculations.

2.5 LUT calculation and Inversion procedure

Table 4 shows the node points for calculating TOA reflectances using a discrete ordinate radiative transfer (DISORT) code of the libRadtran software package (http://libradtran.org) (Mayer and Kylling, 2005). The input options of this radiative transfer model (RTM) to calculate ρ_{TOA} for different aerosol conditions include the spectral phase function and SSA so that the values of each model from AERONET inversion data can be used directly. Note that the input spectral AODs for LUT calculation are normalized to 550 nm using the climatology of each model's Angstrom exponent (AE) between 440 and 870 nm.

The inversion method is adopted from that of Lee et al. (2012). That algorithm retrieves AOD at 550 nm using every MODIS wavelength (470, 555, 650, 860, 1240, 1630, and 2010 nm) and aerosol model, and then select the aerosol model that minimized the standard deviation of the seven different AODs retrieved from each wavelength. The final AOD is chosen from each wavelength. By doing so, each wavelength can contribute equally in selecting the aerosol model. In GOCI YAER algorithm, reference channel is the same as 550 nm and retrieval wavelengths are changed as GOCI wavelengths.

GOCI YAER algorithm retrieves AODs at 550 nm using whole GOCI wavelengths reflectance (412, 443, 490, 555, 660, 680, 745, and 865 nm) and aerosol model over ocean. Final selected wavelengths for retrieving aerosol properties over land are those of which surface reflectances are less than 0.15. If the number of selected wavelengths is greater than or equal to 2, AODs at 550 nm are retrieved from those wavelength and aerosol model. The inversion procedure to retrieve AOD is implemented using interpolation from pre-calculated TOA reflectance at LUT dimensions to observed TOA reflectance according to geometries (solar zenith angle, satellite zenith angle, and relative azimuth angle), assumed aerosol model, wavelength, surface reflectance, and terrain height. Then, 3 aerosol models are selected that

minimized the standard deviation (σ) of the different AODs retrieved from each wavelength, defined as the square root of the average of the squared deviations of the AODs from their average AOD. Final products of AOD, FMF, SSA, and AE are the σ-weighted average value from 3 selected models as below equations:

$$\text{Final AOD at 550 nm} = \sum_{i=1}^{3} C_{Model\,i} \times Averaged\ AOD_{Model\,i}$$

$$C_{Model\,i} = \frac{\frac{1}{\sigma_{Model\,i}}}{\frac{1}{\sigma_{Model\,1}} + \frac{1}{\sigma_{Model\,2}} + \frac{1}{\sigma_{Model\,3}}}$$

Final AE between 440 and 870 nm, FMF at 550 nm, and SSA at 440 nm are determined in the same way except that averaged AOD is replaced with assumed AOPs as in Table 3. The GOCI YAER algorithm classifies a total of six aerosol types using the retrieved final FMF and SSA (Table 5).

3. Case studies of GOCI YAER products during the DRAGON-NE Asia 2012 campaign

Aerosol types of East Asia are very diverse and complicated. Dust occurs sporadically from the Gobi desert and Taklamakan desert of the Continent of Asia and anthropogenic aerosols occur from urban/industrial sites. Highly-absorbing and fine-dominated, non-absorbing and fine-dominated, marine, and dust aerosols are observed similarly over the East Asia (Lee et al., 2014). East China Sea and Yellow Sea are located between the Continent of Asia and the Korean Peninsula so that the long-range transport of aerosols could be detected clearly.

During the DRAGON-NE Asia 2012 campaign, there are high aerosol loading cases. Two representative cases are presented here; the heavy pollution haze case on 6 May, and the dust case on 27 April. On 6 May, 2012, a white haze plume was detected over northeastern China and the Yellow Sea from the true color image as shown in Fig. 6(a). GOCI YAER AOD, FMF, AE, SSA, and aerosol type are plotted in Fig. 6(b)–(f). Note that all pixels regardless of QA values are included in the AOD plot, while only pixels with positive AOD are shown for the other products. High AOD ranging from 1.2 to 2.0 is found at the center of the haze plume, with retrieved FMF and AE of about 0.8 and 1.2, respectively. This means that the haze aerosol is a fine-mode dominant aerosol. The retrieved SSAs at those pixels are in the range 0.955–0.975, corresponding to non-absorbing aerosol. The detected aerosol type of the haze is therefore classified as "Non-absorbing fine" aerosol, shown as blue in Fig. 6(f).

The distribution of FMF, AE, and SSA over land is more inhomogeneous than over ocean, particularly, for pixels with low AOD, which is likely due to the higher surface reflectance, higher spatial variability, and higher uncertainty of land surface reflectance than that of ocean. Nevertheless, it is encouraging that there is less discrepancy between ocean and land, with products showing a continuous distribution across the coastline for both high (~1.0) and low AOD (~0.3) pixels.

Another case is a severe dust case on 27 April, 2012 as shown Fig. 7. Heavy yellow dust plumes are evident in the GOCI true color image. These developed in the Gobi Desert the previous day were transported to the northern part of the Korean Peninsula across the Yellow Sea. The dust plume has a horizontal scale about 1000 km from inland China to the Yellow Sea, with AOD at its center above 2.0 (red color), and about 1.2 at the edge of the plume. The dust plume over the northern part of the Korean Peninsula is mixed with cloud, but the plume

354 in the southern part shows low AOD of about 0.3, with FMF and AE of 0.3 and 0.5,
355 respectively, corresponding to coarse-mode dominated aerosol. SSA ranges from 0.90 to 0.92,
356 corresponding to moderately absorbing aerosol. From the FMF and SSA, the aerosol plume is
357 classified as "Dust", shown as yellow in Fig. 7(f).

358

359 4. Evaluation of GOCI YAER products during the DRAGON-NE Asia 2012
360 campaign

361 Generally, in spring, various aerosol events such as Yellow dust or anthropogenic aerosol
362 occur frequently and intensively over East Asia (Redemann et al., 2003; Schmid et al., 2003;
363 Kim et al., 2007b). Although the campaign was limited to the spring season, it has the
364 advantage of abundant ground-based observations over Korea and Japan. During the
365 campaign, a total of 40 sun photometers were deployed at urban sites and coastal sites. Over
366 the urban areas of Seoul and Osaka, in particular, distances between AERONET sites are
367 about 10 km, which makes validation of satellite data possible at high spatial resolution.

368 MODIS onboard Aqua and Terra provides state-of-the-art global aerosol properties, and its
369 aerosol retrieval algorithms have been developed and improved continuously (Remer et al.,
370 2005; Levy et al., 2007; Hsu et al., 2006). Recently, an updated version was released as C6
371 (Levy et al., 2013; Hsu et al., 2013). MODIS aerosol products consist of dark target (DT)
372 over both ocean and land and deep blue (DB) products over land-only. Their validation
373 against AERONET showed good agreement globally (Levy et al., 2013; Sayer et al., 2013).
374 Because the validation of GOCI using AERONET is limited in spatial coverage, inter-

375 comparison using the satellite-based MODIS dataset is also performed for evaluating the
376 GOCI product.

377 Therefore, GOCI YAER AOD at 550 nm, FMF at 550 nm, SSA at 440 nm, and AE between
378 440 and 870 nm are evaluated using both the ground-based AERONET and satellite-based
379 MODIS datasets.

380 **4.1 Validation conditions between ground-based AERONET and satellite-**
381 **based GOCI and MODIS**

382 For the validation, 38 AERONET sites are selected, which have at least 20 days of
383 observations. The current Level 2.0 version 2 direct-sun all points observation products,
384 inversion products, and the spectral de-convolution algorithm (SDA) products are used in this
385 study (Holben et al., 1998; O'Neill et al., 2003; Dubovik and King, 2000). From the direct
386 sun measurement, AOD and Angstrom exponent are used. The validation for FMF is done
387 using both inversion and SDA products, while the validation for SSA is done using inversion
388 products. Note that the almucantar observation is only possible when the solar zenith angle is
389 greater than 50° (Dubovik et al., 2000), so inversion data are unavailable near noon.

390 Aerosol data from GOCI and AERONET are collocated temporally and spatially for the
391 comparison. The ground-based AERONET observes the sun/sky radiance at intervals of a
392 few minutes at a fixed location, while GOCI observes aerosol over East Asia at hourly
393 intervals. GOCI pixels within 25km of an AERONET site are averaged, and AERONET data
394 within 30 minutes from GOCI observation time are averaged. Comparison is carried out
395 when at least one pixel of GOCI and one temporal value of AERONET exist. Note that
396 AERONET does not observe AOD at 550 nm directly so that it is interpolated from other

channels using a quadratic fit on a log-log scale (Eck et al., 1999). The colocation condition between AERONET and MODIS is the same as for GOCI. Note that validation of MODIS using AERONET is performed for AOD only.

4.2 Inter-comparison condition between MODIS and GOCI

The different characteristics of MODIS and GOCI as LEO and GEO sensors, respectively, need to be considered when inter-comparison is performed. Spatial colocation is based on the fixed grid scale over the GOCI observation area, divided into 0.2° × 0.2° latitude-longitude resolution grid cells. Therefore, MODIS and GOCI data within the same fixed grid are separately averaged, and then matched spatially.

Temporal colocation is based on the MODIS observation time. MODIS level 2 aerosol data are provided as granules, and the maximum difference in scan time in one granule is about 5 minutes. The maximum difference in GOCI scan time for one scene is about 30 minutes, and GOCI scans the observation area every hour. Therefore, two GOCI scenes within 1 hour centered on the MODIS overpass time are interpolated to the MODIS time, and are collocated with MODIS temporally.

4.3 Validation of AOD

The validation involves use of the linear regression equation, and validation metrics including the Pearson's linear correlation coefficient (R), root mean square error (RMSE), mean absolute error (MAE), mean bias error (MBE), and the ratio within expected error (% within EE). Note that MBE and MAE are the mean of differences and absolute differences of value between AERONET and GOCI, respectively. The range of expected error (EE) of AOD is adopted from MODIS DT over land.

Figure 8 compares AOD from GOCI, MODIS DT, and MODIS DB algorithms against AERONET at the 38 DRAGON AERONET sites. Note that only QA = 3 data of MODIS DT and DB AOD are used for validation. A total of 9,602 data points are matched with GOCI for all QA values, and 8,694 for only QA = 3 data. There is good agreement between AERONET and GOCI with high data counts (red color) gathered near the one-to-one line. Because GOCI pixels with QA = 3 are less cloud contaminated than those with all QA values, there are fewer overestimated pixels from the GOCI QA = 3 set. Thus, all validation criteria show better results for QA = 3 than for all QA except for the *y*-intercept of the linear regression line. Most comparison points are concentrated within the EE and immediately below EE in AERONET AOD < 0.4, but large positive biases are observed for AERONET AOD > 0.4, which result in the increase of the *y*-intercept for all QA. Such pixels seem to be contaminated by cloud so, in general, have QA less than 3. Therefore, when only QA = 3 pixels are compared with AERONET, the *y*-intercept has a more negative value of –0.042 than for all QA (0.009). The correlation coefficient for AOD between AERONET and GOCI (QA = 3) is 0.881, which is similar with that of MODIS DT (0.906) and DB (0.876). For slope, RMSE, MBE, and % within EE, GOCI is better than that of MODIS DT. Munchak et al. (2013) described that MODIS DT Collection 6 AOD is biased high over urban surfaces, and it is suspected due to the inaccurate surface reflectance over urban in the MODIS DT operational retrievals. Otherwise, the enhanced MODIS DB algorithm (Collection 6) shows a best result, which controls surface reflectance differently according to surface type, giving high accuracy regardless of surface type (Hsu et al., 2013). The ratio within EE of MODIS DB against AERONET is 71.5% for all AERONET sites, which is greater than for GOCI (57.3%).

442 Results of inter-comparison of AOD between GOCI and MODIS are shown in Fig. 9. Note
443 that ocean pixels near most coastal sites are classified as turbid water and retrieved using the
444 land algorithm. Thus, it is hard to validate the GOCI ocean algorithm using AERONET, but it
445 is possible using MODIS DT ocean AOD. Inter-comparison of the ocean AOD of MODIS
446 DT and GOCI shows good agreement (R = 0.939). The slope of the regression line is 1.019
447 and the y-intercept is 0.039. Both algorithms consider wind speed dependent surface
448 reflectance. Because the ocean surface is darker than the land surface, it is easier to detect
449 cloud pixels over ocean and so there are fewer overestimation points for GOCI. The GOCI
450 AOD over ocean is retrieved from the ocean algorithm over clear water and the land
451 algorithm over turbid water (or heavy aerosol loading). The AOD over turbid water pixels is
452 not retrieved in the MODIS DT ocean algorithm, so direct comparison over turbid water is
453 impossible (Lee et al., 2010b).

454 A common feature of comparisons of GOCI products using MODIS DT and DB over land is
455 that there are more scattered points above the one-to-one line than in comparisons between
456 AERONET and GOCI. Because cloud is effectively cleared in AERONET Level 2 data, most
457 collocated cases with AERONET are in fact cloud-free cases. MODIS DT and DB use the
458 characteristics of cloud in visible and infrared (IR) wavelengths for cloud screening, but there
459 are no IR channels in GOCI so that cloud screening is carried out using visible–near IR
460 channels only. It is more difficult to distinguish the cloud signal clearly over land using only
461 visible characteristics because of bright surface reflectance, especially for urban surfaces. If
462 cloud is not removed correctly, its signal is considered as aerosol, and AOD is overestimated.
463 This explains the greater number of pixels scattered above the one-to-one line in both
464 comparisons over land. GOCI YAER AOD over land is better correlated with MODIS DB (R
465 = 0.866) than DT (R = 0.827), and the linear regression line over land between GOCI and

MODIS DB is also closer to the one-to-one line than with MODIS DT. Although the surface reflectance calculation of GOCI YAER algorithm is not exactly the same as that of MODIS DB algorithm, the methodology of GOCI YAER algorithm is closer with MODIS DB than MODIS DT. Pre-calculated surface reflectance database is applied over Arid-/Semi-arid surfaces, which has been used in previous MODIS DB algorithm (Hsu et al., 2004, 2006) and enhanced MODIS DB algorithm (Hsu et al., 2013). However, enhanced MODIS DB algorithm used in this study for validation adopts three different methods according to land surface types. Over vegetated land surface, it takes the spectral relationship in surface reflectance between visible and longer wavelengths, which is used in the MODIS DT algorithm. Over urban /built-up and transitional regions, a hybrid approach is applied by combining the Deep Blue surface database with the angular shapes of surface BRDF. Aerosol model constructions of three algorithms are similar as the model considers fine/coarse and absorbing/non-absorbing characteristics. But the MODIS DB uses reflectance at 412 nm for retrieval, similar with GOCI, but MODIS DT does not. Inversion procedures of three algorithms are not significantly different. Both MODIS DT and DB retrieve spectral AODs (470 and 660 nm for DT; 412, 470, and 660 nm of DB) and interpolated to the AOD at 550 nm. But GOCI YAER algorithm retrieves AOD at 550 nm directly from other channels reflectance. Hence, the tendency and accuracy of retrieved AOD from GOCI are closer to MODIS DB than DT.

4.4 Validation of Angstrom exponent, fine-mode fraction, and single scattering albedo

The GOCI YAER AE, FMF, and SSA are determined from the three selected aerosol models used in retrieving the AOD. Therefore, the possible product retrieval ranges are limited by the

aerosol models. AE, FMF, and SSA can be retrieved in the ranges of 0.0930–1.744, 0.156–0.956, and 0.871–0.970, respectively.

Figure 10(a) and 10(b) show the comparison of AE between AERONET and GOCI. The correlation coefficient is 0.594 in Fig. 10(a), which is significantly lower than for the AOD comparison (0.881). The difference in spectral aerosol signal does not vary much with aerosol model when AOD is low, so the error of AE can be large at low AOD. When AOD is less than 0.3, the value of AE are about 1.3 for AERONET, but about 0.7 for the GOCI retrieval; thus when these points are removed, the correlation coefficient increases to 0.678 in Fig. 10(b). AE is underestimated from GOCI compared with AERONET (MBE = –0.316) for the whole range although highest density of points from AERONET and GOCI coincide.

Although the MODIS DT AE over land can be calculated using spectral AOD at 470 and 660 nm, inter-comparison of the AE between MODIS DT and GOCI is not done over land in this study. Levy et al. (2010) reported that AE is not available globally at sufficient quantitative accuracy so that it was removed from the operational C6 DT products (Levy et al., 2013). Therefore, comparison is only performed over the ocean. The MODIS DT AOD over the ocean is retrieved at 550 and 860 nm, so the AE between these two channels is compared with the GOCI AE in Fig. 10(c). Over the ocean both GOCI and MODIS DT assume Fresnel reflectance with wind speed dependence for the surface reflectance, and the surface reflectances is similar between GOCI and MODIS DT over, and the surface reflectance of ocean is lower than that of land. Therefore, high counts are well matched and the RMSE and MBE (0.357 and 0.064, respectively) are better than those of AERONET versus GOCI (0.439 and –0.316, respectively) although the correlation coefficient is much lower at 0.376.

511 FMF is provided directly from SDA AERONET, or calculated using the almucantar retrievals
512 of fine AOD and the total AOD at 675 nm from AERONET inversions. Both AERONET
513 FMF products are compared with the GOCI YAER FMF in Fig. 11(a) and 11(b). Note that
514 both comparisons are for AERONET AOD > 0.3. The correlation coefficients are 0.698 and
515 0.750 for SDA and inversion AERONET, respectively. These are higher values than for AE
516 validation, but less than for AOD validation. High counts of AERONET are grouped around
517 0.9–1.0, but those of GOCI are grouped at 0.8. GOCI FMF is underestimated compared with
518 AERONET for the whole FMF range. The MBE values are –0.212 and –0.208, respectively.

519 The inter-comparison of FMF between MODIS DT and GOCI over the ocean is shown in Fig.
520 11(c). The correlation is better (R = 0.417 and RMSE = 0.182) than for of AE (R = 0.376 and
521 RMSE = 0.357). The validation results for FMF are analogous to those of AE because both
522 parameters are sensitive to the particle size in visible wavelengths.

523 Figure 12 shows the results of comparing SSA between AERONET inversion and GOCI.
524 Only 617 points are collocated temporally and spatially because Level 2 AERONET SSA is
525 only provided for AOD (440 nm) > 0.4 and almucantar observation is performed when the
526 solar zenith angle is greater than 50° (Dubovik and King, 2000). The correlation coefficient is
527 0.353, which is the lowest among the GOCI products. Nevertheless, the accuracy of GOCI
528 SSA is comparable with that of OMI SSA over East Asia. According to Jethva et al. (2014),
529 the correlation coefficient between AERONET and OMI SSA is 0.406. They also showed
530 that 44.91% and 70.29% of OMI SSA data are within differences of ±0.03 and ±0.05 with
531 respect to AERONET. GOCI SSA shows higher ratios than OMI, 69.0% and 86.9%, for the
532 same criteria over North East Asia. A preliminary redundancy test (Lee et al., 2012), which
533 showed that GOCI SSA may be underestimated at high SSA (~0.95) and overestimated at

low SSA (~0.85), is consistent with the results of GOCI SSA validation against AERONET. The difference between absorbing and non-absorbing aerosols is significant in the UV and shorter visible (blue) wavelengths, and weak at longer visible (green and red) wavelengths. GOCI YAER algorithm is optimized for AOD retrieval using aerosol model composition classified by FMF and SSA. In the next generation GOCI-2 mission to be launched in 2019, SSA can be retrieved more accurately utilizing UV channel.

GOCI AE and SSA product qualities could be also compared with other previous studies while the region and period are different. Global MODIS DT Angstrom exponent validation results with AERONET were presented in Levy et al. (2010) and Levy et al. (2013) over land and ocean, respectively. Levy et al. (2010) compared MODIS DT Collection 5 Angstrom exponent between 470 and 650 nm (AE_470_650) and AERONET AE_470_650 over land resulted in R of 0.554 and a linear regression equation with MODIS AE_470_660 = 0.6471 × AERONET AE_470_660 + 0.3342. According to Levy et al. (2013), MODIS DT Collection 6 Angstrom exponent between 550 and 870 nm (AE_550_870) shows more higher accuracy over ocean (R = 0.612 and a linear regression equation with MODIS AE_550_870 = 0.686 × AERONET AE_550_870 + 0.47). MODIS DB Collection 6 Angstrom exponent (over land) shows similar accuracy with GOCI YAER Angstrom exponent (R = 0.45 for all AOD and R = 0.68 when AOD is greater than 0.3). These results are similar with that of GOCI YAER AE validation results (R = 0.594 for all AOD and R = 0.678 when AOD is greater than 0.3).

Aerosol optical properties such as Angstrom exponent and single scattering albedo retrieved from the Polarization and Directionality of Earth Reflectance (POLDER) instrument onboard the Polarization and Anisotropy of Reflectances for Atmospheric Science coupled with Observations from a Lidar (PARASOL) satellite shows more accurate results. Hasekamp et al.

(2011) described that AE retrieval using polarization measurement shows higher accuracy (R = 0.85) than using intensity-only retrieval (R = 0.62). Generalized Retrieval of Aerosol & Surface Properties (GRASP) algorithm using POLDER (Dubovik et al., 2011; Kokhanovsky et al., 2015) shows higher accuracy in SSA (R = 0.93) when AOD is greater than 0.4. These results mean that more information such as polarization and multi-angle observation can improve retrieval accuracy of aerosol optical properties. In conclusion, GOCI AE, FMF, and SSA show lower accuracy than AOD. Nevertheless, these values can be useful for qualitative studies, although not for quantitative studies.

5. Error analysis of GOCI YAER AOD

Uncertainties in surface reflectance, assumed aerosol model, cloud masking, and geometry result in systematic errors in the retrieved AOD. In this section, the difference in AOD between GOCI and AERONET is analyzed to quantify the respective error sources affecting the accuracy of GOCI AOD.

The difference in AOD between GOCI and AERONET is shown in Fig. 13(a) as a function of AERONET AOD. The 16%–84% range for each bin widens as AOD increases, as with satellite products. GOCI AOD has a negative bias of –0.1 against AERONET for AERONET AOD < 0.4, while there is no consistent bias but a skewed distribution toward the positive differences for AERONET AOD > 0.9. Main uncertainties in low AOD and high AOD are linked to uncertainties in surface reflectance and assumptions about aerosol microphysical properties, respectively (Sayer et al., 2013). Levy et al. (2010) also described that systematic bias for low AOD results from overestimating the surface reflectance in the visible channels.

579 Therefore, the minimum reflectivity technique can overestimate surface reflectance due to
580 contamination by the remaining cloud or aerosol, resulting in negative bias at low AOD. On
581 the other hand, the accuracy at high AOD can be affected by the assumed aerosol model or
582 cloud masking. An insignificant bias of the median points supports the validity of the
583 assumed aerosol model, but a positive skewed distribution can be attributed to the remaining
584 cloud contamination due to cloud masking using visible channels only. It is difficult to
585 distinguish aerosol and cirrus cloud without information from IR wavelengths (Lee et al.,
586 2013).

587 The next comparison is the difference in AOD between GOCI and AERONET plotted against
588 scattering angle in Fig. 13(b). GOCI AOD is underestimated at scattering angles near 115°
589 and 140° and overestimated at 145° and above 160°. Scattering angle is calculated using solar
590 zenith angle, satellite zenith angle, and relative azimuth angle. GOCI is on geostationary orbit
591 so that satellite zenith and azimuth angle is fixed. Therefore, relative azimuth angle between
592 sun and satellite varies according to local standard time only. Solar zenith angle varies
593 according to local standard time and season. Scattering angle contains such complicate error
594 sources so that scattering angle dependency of AOD difference between GOCI and
595 AERONET is difficult to interpret so that AOD error analyses according to solar zenith angle
596 and relative azimuth angle are also presented.

597 GOCI AOD errors according to solar zenith angle as Fig. 13 (c) are close to zero at 30, 40, 50,
598 and 60° solar zenith angle, and show fluctuating pattern between them. LUT node points of
599 solar zenith angle are constructed at 10° interval, and linear interpolation to observed solar
600 zenith angles in inversion procedure could cause this error pattern. The fluctuation tendency
601 of error as underestimation at scattering angles could be also caused by the interpolation error

in inversion procedure. Subdivision of 5° interval for node point of LUT calculation or online calculation could improve this interpolation error (Jeong et al., 2015).

Error tendency according to relative azimuth angle as Fig. 13 (d) shows less fluctuant shape, and underestimation at low relative azimuth angle. Both conditions of low azimuth angle and high solar zenith angle correspond to the early morning or late afternoon as local standard time. Therefore, errors analyzed according to the fixed local standard time as Fig. 13 (e) shows underestimation at 09:30, 15:30, and 16:30. Plane-parallel atmosphere approximation or scalar calculation in RTM could result in less accurate Rayleigh scattering calculation for surface reflectance using the minimum reflectivity technique.

The method for determining surface reflectance is applied equally to all pixels regardless of surface type. To test the accuracy as a function of surface type, the normalized difference vegetation index (NDVI) is adopted, defined as (ρ_{TOA}(865 nm) − ρ_{TOA}(660 nm)) / (ρ_{TOA}(865 nm) + ρ_{TOA}(660 nm)). Generally, it is negative over ocean and positive over land. It is close to 1 when the surface is green because of vegetation growth, while it is close to zero over less green areas. Figure 13(f) shows the difference in AOD between GOCI and AERONET plotted against NDVI. Note that negative NDVI is possible when GOCI ocean pixels are collocated with AERONET at coastal sites. The difference is small (0–0.05) and the bias is for low NDVI (–0.4 to 0.1). However, the difference decreases linearly from 0.05 to –0.2 as NDVI increases from 0.1 to 0.6, due to the limitation in minimum reflectivity technique with search window of one month during the dynamic vegetation change in the spring season and its reference at 412 nm channel. AOD is significantly underestimated by GOCI with increasing vegetation cover, thus surface type must be considered to improve the algorithm as included in the enhanced MODIS DB algorithm (Hsu et al., 2013). Additionally, this may be

partially due to the most densely vegetated surfaces in both Korea and Japan being forested mountains. Because aerosol concentration decreases exponentially as altitude increases generally, any GOCI retrievals made over the hills or mountains have lower AOD than the values located in the valley or low altitude level area. NDVI is largest over the forested mountain slopes which extend to the upper part of the aerosol layer, therefore the GOCI retrievals are underestimated as NDVI increases.

6. Conclusion

Since its development the prototype over-ocean GOCI YAER algorithm over the ocean (Lee et al., 2010b) was further developed to include non-spherical aerosol models for better performance for dust cases (Lee et al., 2012). However, the algorithm has only been tested using MODIS data, and limited to ocean surfaces. Here, based on the heritage, the GOCI YAER algorithm is extended to land surfaces and tested using real GOCI data. GOCI has the advantages of high spatial (500 m × 500 m) and temporal (hourly) resolution using eight channels in visible and near-infrared wavelengths. Therefore, other properties such as FMF, AE, and SSA as well as AOD can be retrieved at a 6 km × 6 km resolution.

Different surface reflectance assumptions and channels are applied for the land and ocean. Turbid water is detected according to $\Delta\rho_{660}$, and the land algorithm is applied to it for better performance. In addition, nonsphericity and dynamical properties of aerosol are reflected in the aerosol models.

The DRAGON-NE Asia 2012 campaign in spring has enabled the evaluation of GOCI YAER products over 38 sites in Korea and Japan using AERONET data and MODIS over East Asia. AOD from the GOCI YAER shows good agreement with AERONET with a correlation

coefficient of 0.881, which is similar with that of MODIS DT (R = 0.906) and DB (R = 0.876). The fraction of AOD data falling within the expected error for GOCI is 57.3%, which is worse than MODIS DB (71.5%) but similar with MODIS DT (54.2%). In the inter-comparison between GOCI and MODIS, GOCI and MODIS DT show good agreement over ocean with high correlation (R = 0.939). Over land, GOCI YAER shows better agreement and less bias with MODIS DB (R = 0.866, RMSE = 0.192) than MODIS DT (R = 0.827, RMSE = 0.284) likely due in part to similar retrieval conditions in both GOCI and MODIS DB. For size parameters such as AE and FMF, GOCI agrees less well with AEORNET (R = 0.594–0.750) and tends to underestimate (MBE = –0.381 to –0.208). Over ocean, the comparison of size parameters between GOCI and MODIS DT shows significantly poorer agreement (R = 0.376–0.417), but data points with high frequency are well matched. For the SSA, GOCI shows low correlation of 0.353 with AERONET, but the range of SSA (0.90–0.95) is well matched each other. In conclusion, GOCI YAER AOD shows high accuracy against MODIS, and other aerosol parameter products can be used qualitatively although their accuracy is less than AOD.

From the error analysis, GOCI YAER AOD shows a negative bias of –0.1 for low AOD (<0.4), and the negative bias increases as NDVI becomes higher. It is necessary to improve the accuracy of surface reflectance over vegetated areas for the next version, and possibly account for the elevation of forested mountains relative to the aerosol vertical profile.

The current version of LUT was calculated by using a scalar RTM, libRadtran; this RTM is less accurate for calculating Rayleigh scattering for the short visible wavelengths (~400nm). A vector RTM might be helpful in improving the accuracy of the GOCI YAER algorithm in the future. The current validation period is limited to spring season in 2012, and thus the

seasonal dependence of accuracy is not presented in this study. Nearly 4 years of GOCI data have been accumulated since March 2011, which will allow long-term validation and analysis to be carried out to investigate retrieval accuracies and uncertainties in the near future.

Acknowledgements

We thank the Korean Institute of Ocean Science and Technology (KIOST) for the development and application of GOCI in this research. We also thank all PI investigators and their staff for establishing and maintaining the AERONET sites of DRAGON-NE Asia 2012 campaign used in this investigation. We also thank the MODIS science team for providing valuable data for this research. This research was supported by the GEMS program of the Ministry of Environment, Korea, and the Eco Innovation Program of KEITI (2012000160002).

683 **References**

684 Ahn, J. H., Park, Y. J., Ryu, J. H., Lee, B., and Oh, I. S.: Development of Atmospheric
685 Correction Algorithm for Geostationary Ocean Color Imager (GOCI), Ocean Sci J, 47, 247-
686 259, 2012.

687 Choi, J. K., Park, Y. J., Ahn, J. H., Lim, H. S., Eom, J., and Ryu, J. H.: GOCI, the world's
688 first geostationary ocean color observation satellite, for the monitoring of temporal variability
689 in coastal water turbidity, J Geophys Res-Oceans, 117, C09004,
690 doi:09010.01029/02012JC008046, 2012.

691 Ciren, P. and Kondragunta, S.: Dust aerosol index (DAI) algorithm for MODIS, J Geophys
692 Res-Atmos, 119, 4770-4792, 2014.

693 Cox, C. and Munk, W.: Statistics of the sea surface derived from sun glitter, Journal of
694 Marine Research, 13, 198-227, 1954.

695 Dubovik, O. and King, M. D.: A flexible inversion algorithm for retrieval of aerosol optical
696 properties from Sun and sky radiance measurements, J Geophys Res-Atmos, 105, 20673-
697 20696, 2000.

698 Dubovik, O., Smirnov, A., Holben, B. N., King, M. D., Kaufman, Y. J., Eck, T. F., and
699 Slutsker, I.: Accuracy assessments of aerosol optical properties retrieved from Aerosol
700 Robotic Network (AERONET) Sun and sky radiance measurements, J Geophys Res-Atmos,
701 105, 9791-9806, 2000.

702 Dubovik, O., Sinyuk, A., Lapyonok, T., Holben, B. N., Mishchenko, M., Yang, P., Eck, T. F.,
703 Volten, H., Munoz, O., Veihelmann, B., van der Zande, W. J., Leon, J. F., Sorokin, M., and
704 Slutsker, I.: Application of spheroid models to account for aerosol particle nonsphericity in
705 remote sensing of desert dust, J Geophys Res-Atmos, 111, D11208,
706 doi:11210.11029/12005JD006619, 2006.

707 Dubovik, O., Herman, M., Holdak, A., Lapyonok, T., Tanré, D., Deuzé, J. L., Ducos, F.,
708 Sinyuk, A., and Lopatin, A.: Statistically optimized inversion algorithm for enhanced
709 retrieval of aerosol properties from spectral multi-angle polarimetric satellite observations,
710 Atmos. Meas. Tech., 4, 975-1018, 2011.
711 Eck, T. F., Holben, B. N., Reid, J. S., Dubovik, O., Smirnov, A., O'Neill, N. T., Slutsker, I.,
712 and Kinne, S.: Wavelength dependence of the optical depth of biomass burning, urban, and
713 desert dust aerosols, J Geophys Res-Atmos, 104, 31333-31349, 1999.
714 Eck, T. F., Holben, B. N., Reid, J. S., O'Neill, N. T., Schafer, J. S., Dubovik, O., Smirnov, A.,
715 Yamasoe, M. A., and Artaxo, P.: High aerosol optical depth biomass burning events: A
716 comparison of optical properties for different source regions, Geophys Res Lett, 30, 2035,
717 doi:2010.1029/2003GL017861, 2003.
718 Fukuda, S., Nakajima, T., Takenaka, H., Higurashi, A., Kikuchi, N., Nakajima, T. Y., and
719 Ishida, H.: New approaches to removing cloud shadows and evaluating the 380 nm surface
720 reflectance for improved aerosol optical thickness retrievals from the GOSAT/TANSO-Cloud
721 and Aerosol Imager, Journal of Geophysical Research: Atmospheres, 118, 13520-13531,
722 2013.
723 Hasekamp, O. P., Litvinov, P., and Butz, A.: Aerosol properties over the ocean from
724 PARASOL multiangle photopolarimetric measurements, Journal of Geophysical Research:
725 Atmospheres, 116, D14204, doi:14210.11029/12010JD015469, 2011.
726 Herman, J. R. and Celarier, E. A.: Earth surface reflectivity climatology at 340-380 nm from
727 TOMS data, J Geophys Res-Atmos, 102, 28003-28011, 1997.
728 Higurashi, A. and Nakajima, T.: Development of a two-channel aerosol retrieval algorithm on
729 a global scale using NOAA AVHRR, J Atmos Sci, 56, 924-941, 1999.
730 Holben, B. N., Eck, T. F., Slutsker, I., Tanre, D., Buis, J. P., Setzer, A., Vermote, E., Reagan,

731 J. A., Kaufman, Y. J., Nakajima, T., Lavenu, F., Jankowiak, I., and Smirnov, A.: AERONET
732 - A federated instrument network and data archive for aerosol characterization, Remote Sens
733 Environ, 66, 1-16, 1998.
734 Hsu, N. C., Tsay, S. C., King, M. D., and Herman, J. R.: Aerosol properties over bright-
735 reflecting source regions, Ieee T Geosci Remote, 42, 557-569, 2004.
736 Hsu, N. C., Tsay, S. C., King, M. D., and Herman, J. R.: Deep blue retrievals of Asian
737 aerosol properties during ACE-Asia, Ieee T Geosci Remote, 44, 3180-3195, 2006.
738 Hsu, N. C., Gautam, R., Sayer, A. M., Bettenhausen, C., Li, C., Jeong, M. J., Tsay, S. C., and
739 Holben, B. N.: Global and regional trends of aerosol optical depth over land and ocean using
740 SeaWiFS measurements from 1997 to 2010, Atmos Chem Phys, 12, 8037-8053, 2012.
741 Hsu, N. C., Jeong, M. J., Bettenhausen, C., Sayer, A. M., Hansell, R., Seftor, C. S., Huang, J.,
742 and Tsay, S. C.: Enhanced Deep Blue aerosol retrieval algorithm: The second generation, J
743 Geophys Res-Atmos, 118, 9296-9315, 2013.
744 IPCC: Climate Change 2013: The Physical Science Basis. Contribution of Working Group I
745 to the Fifth Assessment Report of the Intergovernmental Panel on Climate Change,
746 Cambridge University Press, Cambridge, United Kingdom and New York, NY, USA, 2013.
747 Jackson, J. M., Liu, H. Q., Laszlo, I., Kondragunta, S., Remer, L. A., Huang, J. F., and Huang,
748 H. C.: Suomi-NPP VIIRS aerosol algorithms and data products, J Geophys Res-Atmos, 118,
749 12673-12689, 2013.
750 Jeong, U., Kim, J., Ahn, C., Torres, O., Liu, X., Bhartia, P. K., Spurr, R. J. D., Haffner, D.,
751 Chance, K., and Holben, B. N.: An online aerosol retrieval algorithm using OMI near-UV
752 observations based on the optimal estimation method, Atmos. Chem. Phys. Discuss., 15,
753 16615-16654, 2015.
754 Jethva, H., Torres, O., and Ahn, C.: Global assessment of OMI aerosol single-scattering

albedo using ground-based AERONET inversion, J Geophys Res-Atmos, 119, 9020-9040, 2014.

Kang, G., Youn, H. S., Choi, S. B., and Coste, P.: Radiometric calibration of COMS geostationary ocean color imager, in: Sensors, Systems, and Next-Generation Satellites X, Proc. SPIE, Stockholm, Sweden, doi: 10.1117/12.689888, 2006.

Kaufman, Y. J., Tanre, D., Remer, L. A., Vermote, E. F., Chu, A., and Holben, B. N.: Operational remote sensing of tropospheric aerosol over land from EOS moderate resolution imaging spectroradiometer, J Geophys Res-Atmos, 102, 17051-17067, 1997a.

Kaufman, Y. J., Wald, A. E., Remer, L. A., Gao, B. C., Li, R. R., and Flynn, L.: The MODIS 2.1-mu m channel - Correlation with visible reflectance for use in remote sensing of aerosol, Ieee T Geosci Remote, 35, 1286-1298, 1997b.

Kim, J., Lee, J., Lee, H. C., Higurashi, A., Takemura, T., and Song, C. H.: Consistency of the aerosol type classification from satellite remote sensing during the Atmospheric Brown Cloud-East Asia Regional Experiment campaign, J Geophys Res-Atmos, 112, D22S33, doi:10.1029/2006JD008201, 2007a.

Kim, J., Yoon, J. M., Ahn, M. H., Sohn, B. J., and Lim, H. S.: Retrieving aerosol optical depth using visible and mid-IR channels from geostationary satellite MTSAT-1R, Int J Remote Sens, 29, 6181-6192, 2008.

Kim, S. W., Yoon, S. C., Kim, J., and Kim, S. Y.: Seasonal and monthly variations of columnar aerosol optical properties over east Asia determined from multi-year MODIS, LIDAR, and AERONET Sun/sky radiometer measurements, Atmos Environ, 41, 1634-1651, 2007b.

Knapp, K. R., Vonder Haar, T. H., and Kaufman, Y. J.: Aerosol optical depth retrieval from GOES-8: Uncertainty study and retrieval validation over South America, J Geophys Res-

779 Atmos, 107, 4055, doi:4010.1029/2001JD000505, 2002.
780 Knapp, K. R., Frouin, R., Kondragunta, S., and Prados, A.: Toward aerosol optical depth
781 retrievals over land from GOES visible radiances: determining surface reflectance, Int J
782 Remote Sens, 26, 4097-4116, 2005.
783 Koelemeijer, R. B. A., de Haan, J. F., and Stammes, P.: A database of spectral surface
784 reflectivity in the range 335-772 nm derived from 5.5 years of GOME observations, J
785 Geophys Res-Atmos, 108, 4070, doi:4010.1029/2002jd002429, 2003.
786 Kokhanovsky, A. A., Davis, A. B., Cairns, B., Dubovik, O., Hasekamp, O. P., Sano, I.,
787 Mukai, S., Rozanov, V. V., Litvinov, P., Lapyonok, T., Kolomiets, I. S., Oberemok, Y. A.,
788 Savenkov, S., Martin, W., Wasilewski, A., Di Noia, A., Stap, F. A., Rietjens, J., Xu, F.,
789 Natraj, V., Duan, M., Cheng, T., and Munro, R.: Space-based remote sensing of atmospheric
790 aerosols: The multi-angle spectro-polarimetric frontier, Earth-Science Reviews, 145, 85-116,
791 2015.
792 Lee, J., Kim, J., Song, C. H., Kim, S. B., Chun, Y., Sohn, B. J., and Holben, B. N.:
793 Characteristics of aerosol types from AERONET sunphotometer measurements, Atmos
794 Environ, 44, 3110-3117, 2010a.
795 Lee, J., Kim, J., Song, C. H., Ryu, J. H., Ahn, Y. H., and Song, C. K.: Algorithm for retrieval
796 of aerosol optical properties over the ocean from the Geostationary Ocean Color Imager,
797 Remote Sens Environ, 114, 1077-1088, 2010b.
798 Lee, J., Kim, J., Yang, P., and Hsu, N. C.: Improvement of aerosol optical depth retrieval
799 from MODIS spectral reflectance over the global ocean using new aerosol models archived
800 from AERONET inversion data and tri-axial ellipsoidal dust database, Atmos Chem Phys, 12,
801 7087-7102, 2012.
802 Lee, J., Hsu, N. C., Bettenhausen, C., and Sayer, A. M.: Retrieval of aerosol optical depth

803 under thin cirrus from MODIS: Application to an ocean algorithm, J Geophys Res-Atmos,
804 118, 10111-10124, 2013.
805 Lee, J., Kim, J., and Lee, Y. G.: Simultaneous retrieval of aerosol properties and clear-sky
806 direct radiative effect over the global ocean from MODIS, Atmos Environ, 92, 309-317, 2014.
807 Levy, R. C., Remer, L. A., Mattoo, S., Vermote, E. F., and Kaufman, Y. J.: Second-
808 generation operational algorithm: Retrieval of aerosol properties over land from inversion of
809 Moderate Resolution Imaging Spectroradiometer spectral reflectance, J Geophys Res-Atmos,
810 112, D13211, doi:13210.11029/12006jd007811, 2007.
811 Levy, R. C., Remer, L. A., Kleidman, R. G., Mattoo, S., Ichoku, C., Kahn, R., and Eck, T. F.:
812 Global evaluation of the Collection 5 MODIS dark-target aerosol products over land, Atmos
813 Chem Phys, 10, 10399-10420, 2010.
814 Levy, R. C., Mattoo, S., Munchak, L. A., Remer, L. A., Sayer, A. M., Patadia, F., and Hsu, N.
815 C.: The Collection 6 MODIS aerosol products over land and ocean, Atmos Meas Tech, 6,
816 2989-3034, 2013.
817 Li, R. R., Kaufman, Y. J., Gao, B. C., and Davis, C. O.: Remote sensing of suspended
818 sediments and shallow coastal waters, Ieee T Geosci Remote, 41, 559-566, 2003.
819 Mayer, B. and Kylling, A.: Technical note: The libRadtran software package for radiative
820 transfer calculations - description and examples of use, Atmos Chem Phys, 5, 1855-1877,
821 2005.
822 Mishchenko, M. I., Travis, L. D., Kahn, R. A., and West, R. A.: Modeling phase functions for
823 dustlike tropospheric aerosols using a shape mixture of randomly oriented polydisperse
824 spheroids, J Geophys Res-Atmos, 102, 16831-16847, 1997.
825 Munchak, L. A., Levy, R. C., Mattoo, S., Remer, L. A., Holben, B. N., Schafer, J. S.,
826 Hostetler, C. A., and Ferrare, R. A.: MODIS 3 km aerosol product: applications over land in

827 an urban/suburban region, Atmos Meas Tech, 6, 1747-1759, 2013.
828 O'Neill, N. T., Eck, T. F., Smirnov, A., Holben, B. N., and Thulasiraman, S.: Spectral
829 discrimination of coarse and fine mode optical depth, J Geophys Res-Atmos, 108, 4559,
830 doi:4510.1029/2002jd002975, 2003.
831 Park, M. E., Song, C. H., Park, R. S., Lee, J., Kim, J., Lee, S., Woo, J. H., Carmichael, G. R.,
832 Eck, T. F., Holben, B. N., Lee, S. S., Song, C. K., and Hong, Y. D.: New approach to monitor
833 transboundary particulate pollution over Northeast Asia, Atmos Chem Phys, 14, 659-674,
834 2014.
835 Redemann, J., Masonis, S. J., Schmid, B., Anderson, T. L., Russell, P. B., Livingston, J. M.,
836 Dubovik, O., and Clarke, A. D.: Clear-column closure studies of aerosols and water vapor
837 aboard the NCAR C-130 during ACE-Asia, 2001, J Geophys Res-Atmos, 108, 8655,
838 doi:8610.1029/2003jd003442, 2003.
839 Reid, J. S., Hobbs, P. V., Ferek, R. J., Blake, D. R., Martins, J. V., Dunlap, M. R., and
840 Liousse, C.: Physical, chemical, and optical properties of regional hazes dominated by smoke
841 in Brazil, J Geophys Res-Atmos, 103, 32059-32080, 1998.
842 Remer, L. A., Kaufman, Y. J., Tanré, D., Mattoo, S., Chu, D. A., Martins, J. V., Li, R. R.,
843 Ichoku, C., Levy, R. C., Kleidman, R. G., Eck, T. F., Vermote, E., and Holben, B. N.: The
844 MODIS Aerosol Algorithm, Products, and Validation, J Atmos Sci, 62, 947-973, 2005.
845 Remer, L. A., Kleidman, R. G., Levy, R. C., Kaufman, Y. J., Tanre, D., Mattoo, S., Martins, J.
846 V., Ichoku, C., Koren, I., Yu, H. B., and Holben, B. N.: Global aerosol climatology from the
847 MODIS satellite sensors, J Geophys Res-Atmos, 113, D14s07, doi:10.1029/2007jd009661,
848 2008.
849 Saide, P. E., Kim, J., Song, C. H., Choi, M., Cheng, Y. F., and Carmichael, G. R.:
850 Assimilation of next generation geostationary aerosol optical depth retrievals to improve air

quality simulations, Geophys Res Lett, 41, 9188-9196, 2014.

Sayer, A. M., Hsu, N. C., Bettenhausen, C., Ahmad, Z., Holben, B. N., Smirnov, A., Thomas, G. E., and Zhang, J.: SeaWiFS Ocean Aerosol Retrieval (SOAR): Algorithm, validation, and comparison with other data sets, J Geophys Res-Atmos, 117, D03206, doi:03210.01029/02011jd016599, 2012.

Sayer, A. M., Hsu, N. C., Bettenhausen, C., and Jeong, M. J.: Validation and uncertainty estimates for MODIS Collection 6 "Deep Blue" aerosol data, J Geophys Res-Atmos, 118, 7864-7872, 2013.

Schmid, B., Hegg, D. A., Wang, J., Bates, D., Redemann, J., Russell, P. B., Livingston, J. M., Jonsson, H. H., Welton, E. J., Seinfeld, J. H., Flagan, R. C., Covert, D. S., Dubovik, O., and Jefferson, A.: Column closure studies of lower tropospheric aerosol and water vapor during ACE-Asia using airborne Sun photometer and airborne in situ and ship-based lidar measurements, J Geophys Res-Atmos, 108, 8656, doi:8610.1029/2002jd003361, 2003.

Torres, O., Bhartia, P. K., Herman, J. R., Ahmad, Z., and Gleason, J.: Derivation of aerosol properties from satellite measurements of backscattered ultraviolet radiation: Theoretical basis, J Geophys Res-Atmos, 103, 17099-17110, 1998.

Torres, O., Tanskanen, A., Veihelmann, B., Ahn, C., Braak, R., Bhartia, P. K., Veefkind, P., and Levelt, P.: Aerosols and surface UV products from Ozone Monitoring Instrument observations: An overview, J Geophys Res-Atmos, 112, D24s47, doi:10.1029/2007jd008809, 2007.

Torres, O., Jethva, H., and Bhartia, P. K.: Retrieval of Aerosol Optical Depth above Clouds from OMI Observations: Sensitivity Analysis and Case Studies, J Atmos Sci, 69, 1037-1053, 2012.

Urm, Y.-D. and Sohn, B.-J.: Estimation of aerosol optical thickness over east asia using

875 GMS-5 visible channel measurements, Journal of Atmosphere, 15, 203-211, 2005.
876 von Hoyningen-Huene, W., Freitag, M., and Burrows, J. B.: Retrieval of aerosol optical
877 thickness over land surfaces from top-of-atmosphere radiance, Journal of Geophysical
878 Research: Atmospheres, 108, doi: 10.1029/2001JD002018, 2003.
879 von Hoyningen-Huene, W., Yoon, J., Vountas, M., Istomina, L. G., Rohen, G., Dinter, T.,
880 Kokhanovsky, A. A., and Burrows, J. P.: Retrieval of spectral aerosol optical thickness over
881 land using ocean color sensors MERIS and SeaWiFS, Atmos Meas Tech, 4, 151-171, 2011.
882 Wang, J., Christopher, S. A., Brechtel, F., Kim, J., Schmid, B., Redemann, J., Russell, P. B.,
883 Quinn, P., and Holben, B. N.: Geostationary satellite retrievals of aerosol optical thickness
884 during ACE-Asia, J Geophys Res-Atmos, 108, 8657, doi:8610.1029/2003jd003580, 2003.
885 Xu, J. W., Martin, R. V., van Donkelaar, A., Kim, J., Choi, M., Zhang, Q., Geng, G., Liu, Y.,
886 Ma, Z., Huang, L., Wang, Y., Chen, H., Che, H., Lin, P., and Lin, N.: Estimating ground-
887 level PM2.5 in eastern China using aerosol optical depth determined from the GOCI satellite
888 instrument, Atmos. Chem. Phys., 15, 13133-13144, 2015.
889 Yoon, J., von Hoyningen-Huene, W., Vountas, M., and Burrows, J. P.: Analysis of linear
890 long-term trend of aerosol optical thickness derived from SeaWiFS using BAER over Europe
891 and South China, Atmos. Chem. Phys., 11, 12149-12167, 2011.
892 Yoon, J., von Hoyningen-Huene, W., Kokhanovsky, A. A., Vountas, M., and Burrows, J. P.:
893 Trend analysis of aerosol optical thickness and Ångström exponent derived from the global
894 AERONET spectral observations, Atmos. Meas. Tech., 5, 1271-1299, 2012.
895 Yoon, J., Burrows, J. P., Vountas, M., von Hoyningen-Huene, W., Chang, D. Y., Richter, A.,
896 and Hilboll, A.: Changes in atmospheric aerosol loading retrieved from space-based
897 measurements during the past decade, Atmos Chem Phys, 14, 6881-6902, 2014.
898 Yoon, J. M., Kim, J., Lee, J. H., Cho, H. K., Sohn, B. J., and Ahn, M. H.: Retrieval of

899 Aerosol Optical Depth over East Asia from a Geostationary Satellite, MTSAT-1R, Asia-Pac J
900 Atmos Sci, 43, 133-142, 2007.
901 Zhang, H., Lyapustin, A., Wang, Y., Kondragunta, S., Laszlo, I., Ciren, P., and Hoff, R. M.:
902 A multi-angle aerosol optical depth retrieval algorithm for geostationary satellite data over
903 the United States, Atmos. Chem. Phys., 11, 11977-11991, 2011.

904

905 Table 1. The specification of ocean color sensors.

Sensor	CZCS	SeaWiFS	MERIS	MODIS	GOCI
Platform	Nimbus-7	OrbView-2	Envisat	Terra/ Aqua	COMS
Period	24 Oct 1978 – 01 Aug 1994	01 Aug 1997 – 11 Dec 2010	01 Mar 2002 – 08 Apr 2012	18 Dec 1999 - current (Terra) 04 May 2002 - current (Aqua)	26 June 2010 - current
Orbit type	LEO (Sun-synchronous orbit)	LEO (Sun-synchronous orbit)	LEO (Sun-synchronous orbit)	LEO (Sun-synchronous orbit)	GEO
Local equatorial crossing time (only for LEO), or Longitude (only for GEO)	12:00 Descending node	12:00 Descending node	10:00 Descending node	10:30 Descending node (Terra) 13:30 Ascending node (Aqua)	128.2° E

Swath (only for LEO)	1600 km	2800 km	1150 km	2230 km	
Coverage / Cycle	Near-global coverage every day	Global coverage everyday	Global coverage in 3 days	Global coverage nearly twice/day (long-wave channels) or once/day (short-wave channels)	Area of 2500 km x 2500 km / hourly in daylight (8 times per day)
Spatial resolution	825 m	1100 m	300 m (Europe) 1200 m (Global)	1000 m	500 m
No. of ocean color channels	6	8	15	9 (total 36 channels)	8
Center wavelengths (and band width) of	443 (20) 520 (20) 550 (20) 670 (20)	412 (20) 443 (20) 490 (20) 510 (20)	412.5 (10) 442.5 (10) 490 (10) 510 (10)	412 (15) 443 (10) 488 (10) 531 (10)	412 (20) 443 (20) 490 (20) 555 (20)

ocean color bands (nm)	750 (100) 1150 (1000)	555 (20) 670 (20) 765 (40) 865 (40)	560 (10) 620 (10) 665 (10) 681.25 (7.5) 708.75 (10) 760.625 (3.75) 778.75 (15) 865 (20) 885 (10) 900 (10)	551 (10) 667 (10) 678 (10) 748 (10) 870 (15) (Only ocean color bands are presented.)	660 (20) 680 (10) 745 (20) 865 (40)

908 Table 2. Conditions for determining pixel QA values from 0 to 3.

QA	Number of pixels (N) selected from possible 12 x 12 pixels	Range of retrieved AOD at 550 nm
0	$6 \leq N \leq 14$	$-0.10 \leq AOD < 0.05$, or $3.6 < AOD \leq 5.0$
1	$15 \leq N \leq 21$	$-0.05 \leq AOD \leq 3.6$
2	$22 \leq N \leq 35$	$-0.05 \leq AOD \leq 3.6$
3	$36 \leq N \leq 58$ (maximum)	$-0.05 \leq AOD \leq 3.6$

909

910

911 Table 3. The number of AERONET inversion data, and considering AE between 440 and 870
912 nm, FMF at 550 nm, and SSA at 440 nm for the 26 aerosol models. The minimum and
913 maximum values are shown because of AOD dependence. “H”, “M”, and “N” mean “Highly
914 absorbing”, “Moderately absorbing”, and “Non-absorbing” models, respectively.

		FMF (550 nm)								
		0.1–0.2	0.2–0.3	0.3–0.4	0.4–0.5	0.5–0.6	0.6–0.7	0.7–0.8	0.8–0.9	0.9–1.0
SSA (440 nm)	0.85-0.90	H1	H2	H3	H4	H5	H6	H7	H8	H9
		3298	4309	1960	1360	1151	1256	2145	3420	1933
		0.094-0.184	0.336-0.366	0.563-0.632	0.674-0.855	0.832-1.065	1.140-1.239	1.230-1.430	1.305-1.569	1.570-1.617
		0.156-0.173	0.243-0.247	0.339-0.345	0.447-0.448	0.541-0.553	0.647-0.652	0.756-0.758	0.852-0.857	0.928-0.934
		0.883-0.886	0.880-0.881	0.871-0.881	0.874-0.877	0.876-0.879	0.877-0.882	0.876-0.879	0.880-0.881	0.880-0.884
	0.90-0.95	M1	M2	M3	M4	M5	M6	M7	M8	M9
		5699	6111	2396	1606	1185	1431	2344	5520	6641
		0.132-0.182	0.278-0.366	0.421-0.638	0.408-0.868	0.765-1.070	1.082-1.270	1.203-1.452	1.276-1.623	1.563-1.648
		0.165-0.174	0.227-0.246	0.340-0.350	0.445-0.447	0.548-0.552	0.649-0.652	0.754-0.755	0.856-0.863	0.934-0.946
		0.918-0.920	0.920-0.921	0.921-0.922	0.922-0.922	0.917-0.923	0.915-0.923	0.919-0.926	0.920-0.927	0.927-0.930

		N1	N2	N3	N4	N5	N6	N7	N8
		558	366	289	279	382	845	2643	7585
0.95-1.00		0.276-0.380	0.464-0.645	0.452-0.877	0.711-1.065	1.032-1.275	1.191-1.464	1.258-1.652	1.426-1.744
		0.230-0.248	0.344-0.350	0.441-0.448	0.546-0.555	0.654-0.658	0.756-0.759	0.860-0.869	0.941-0.956
		0.958-0.965	0.961-0.965	0.959-0.967	0.957-0.965	0.961-0.967	0.959-0.968	0.962-0.969	0.967-0.970

915

916

917 Table 4. LUT dimensions.

Variable	Number of entries	Entries
Wavelength	8	412, 443, 490, 555, 660, 680, 765, 870 nm (considering spectral response function)
Solar zenith angle	8	0, 10, …, 70° (10° interval)
Satellite zenith angle	8	0, 10, …, 70° (10° interval)
Relative azimuth angle	19	0, 10, …, 180° (10° interval)
AOD	9	0.0, 0.1, 0.3, 0.6, 1.0, 1.5, 2.1, 2.8, 3.6 at 550 nm
Aerosol model	26	In table 2.
Surface reflectance (only for land LUT)	4	0.0, 0.1, 0.2
Terrain height (only for land LUT)	2	0 km, 5 km
Wind speed (only for ocean LUT)	6	1, 3, 5, 7, 9, and 20 m/s

918

919

920 Table 5. Output aerosol types for GOCI YAER according to FMF and SSA.

No.	Aerosol Type	FMF (550 nm)	SSA (440 nm)
1	Dust	$0.0 \leq FMF < 0.4$	$SSA \leq 0.95$
2	Non-absorbing coarse type	$0.0 \leq FMF < 0.4$	$0.95 < SSA < 1.00$
3	Mixture	$0.4 \leq FMF < 0.6$	
4	Highly-absorbing fine type	$0.6 \leq FMF < 1.0$	$SSA < 0.90$
5	Moderately-absorbing fine type	$0.6 \leq FMF < 1.0$	$0.90 \leq SSA < 0.95$
6	Non-absorbing fine type	$0.6 \leq FMF < 1.0$	$SSA \geq 1.00$

921

922

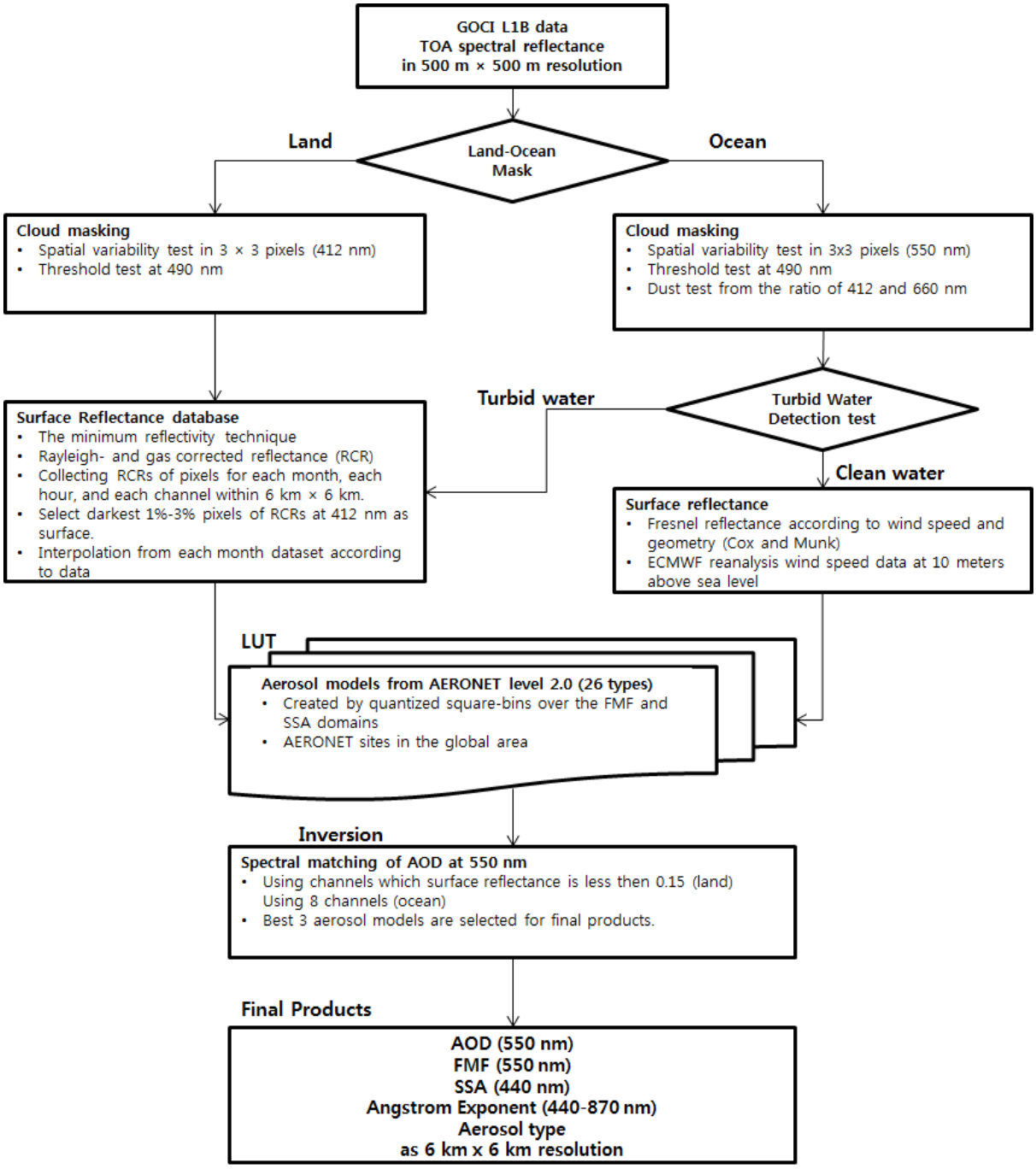

Figure 1. Flow-chart for GOCI YAER algorithm.

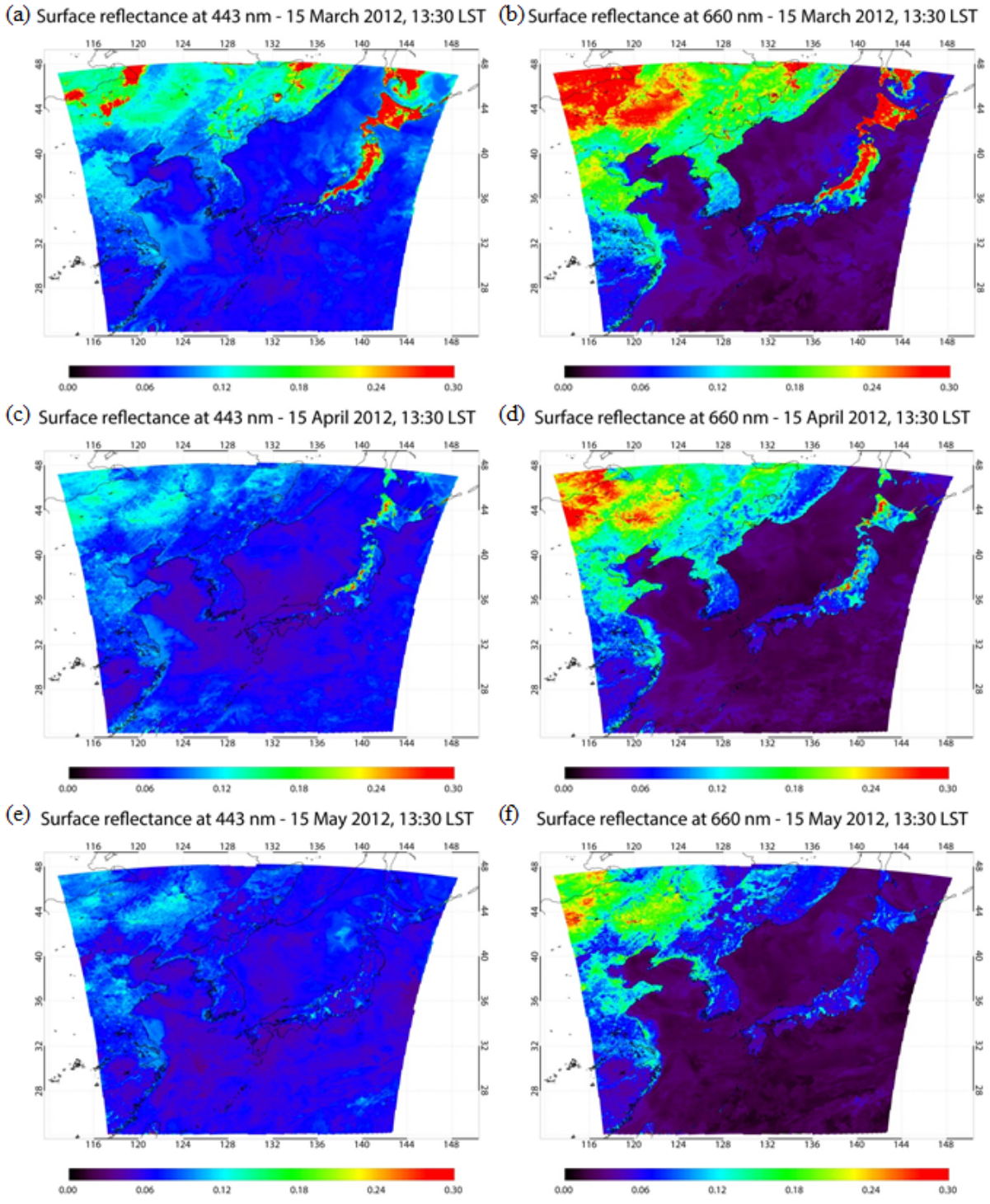

927

928 Figure 2. Surface reflectance on 15th of the month, 13:30 local standard time (LST) at 443 nm
929 (left column) and 660 nm (right column): March (upper row), April (middle row), and May
930 (lower row).

931

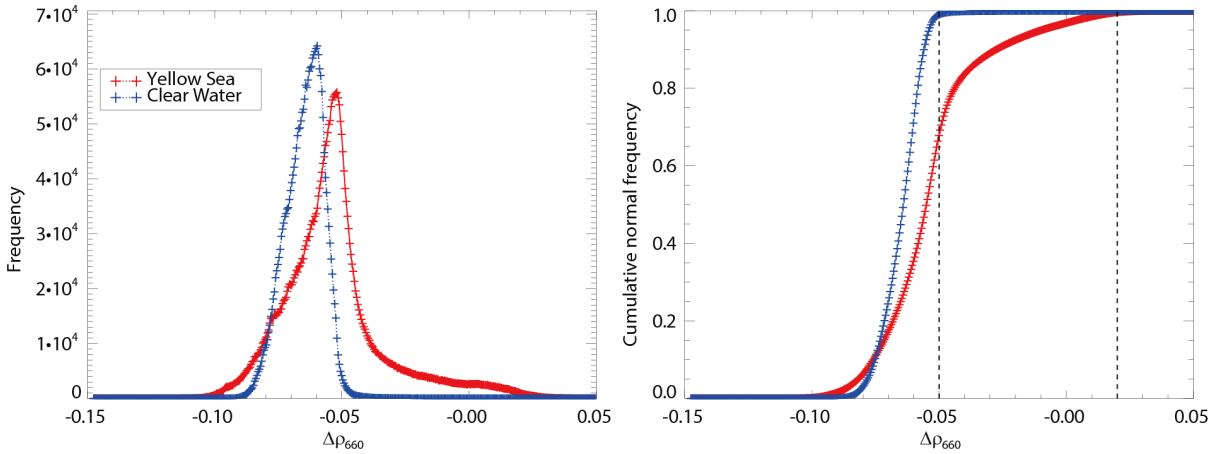

932

933 Figure 3. Frequency and cumulative normal frequency of $\Delta\rho_{660}$ over the Yellow Sea and

934 over clear water.

935

936

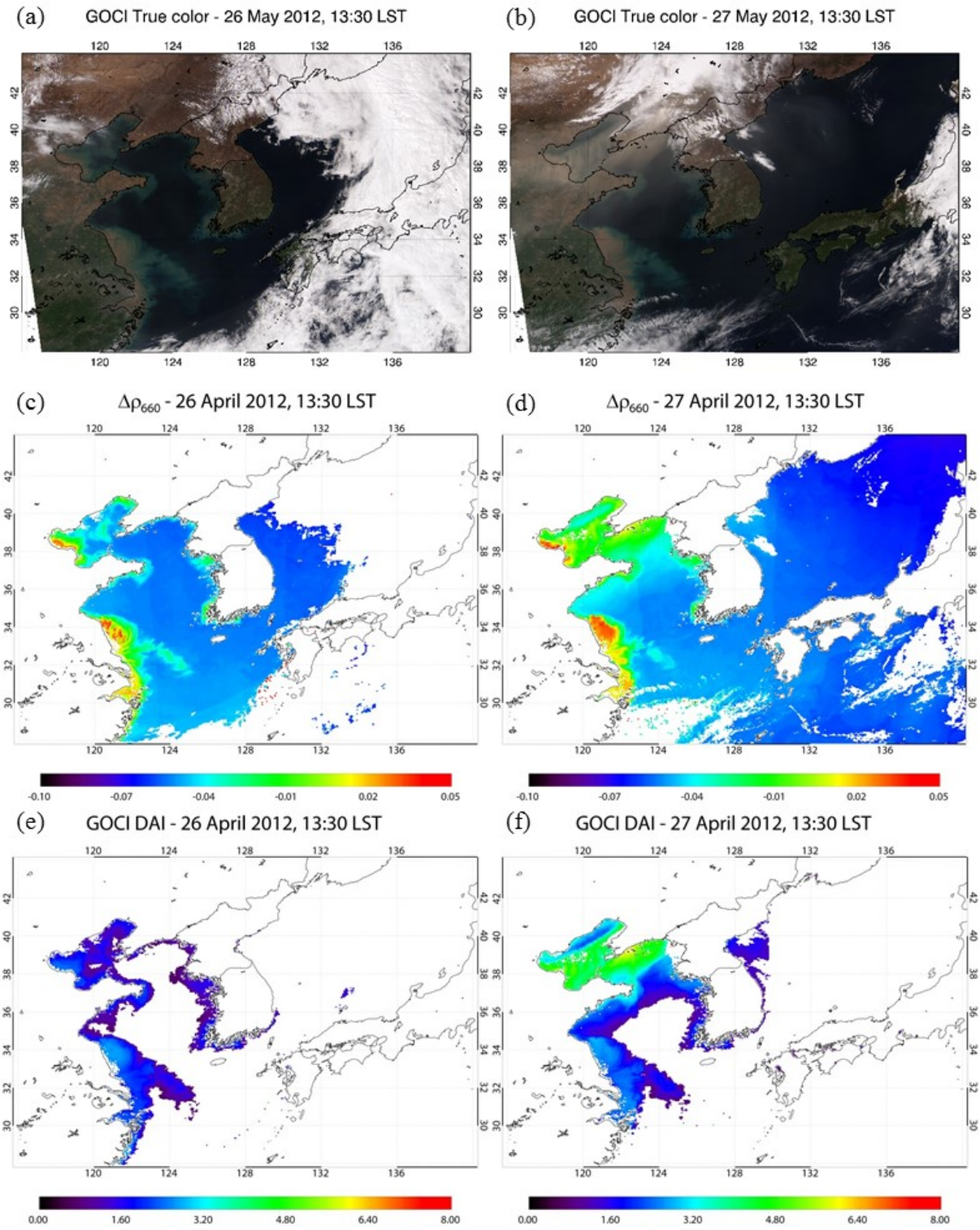

Figure 4. $\Delta\rho_{660}$ and DAI images at 13:30 LST on (a), (b) 26 April 2012 (No dust case) and (c), (d) the following day (Dust case), respectively.

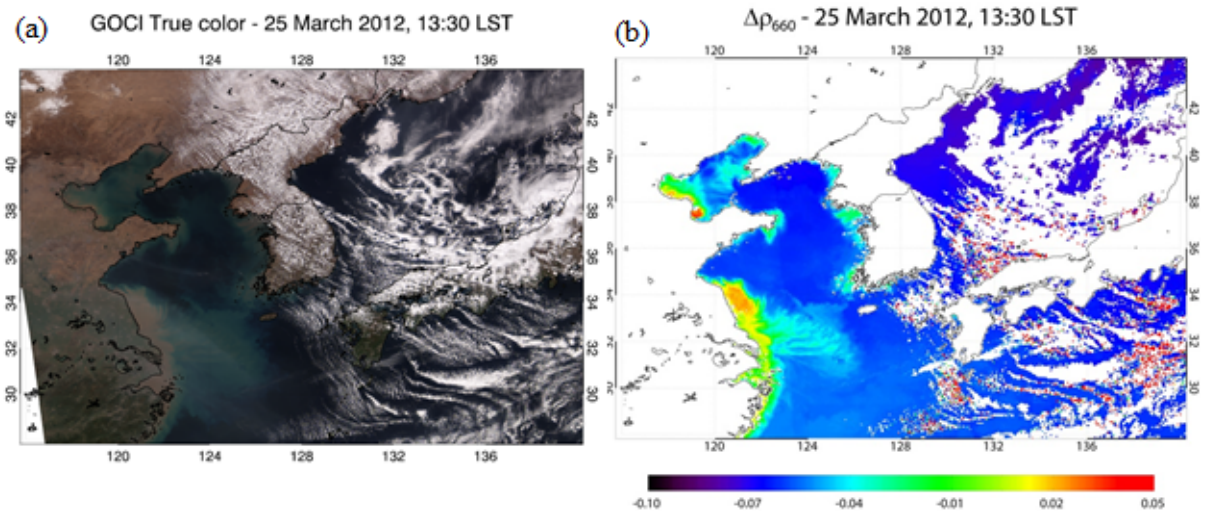

940

941 Figure 5. 25 March 2012, 13:30 LST (a) true color image and (b) $\Delta\rho_{660}$.

942

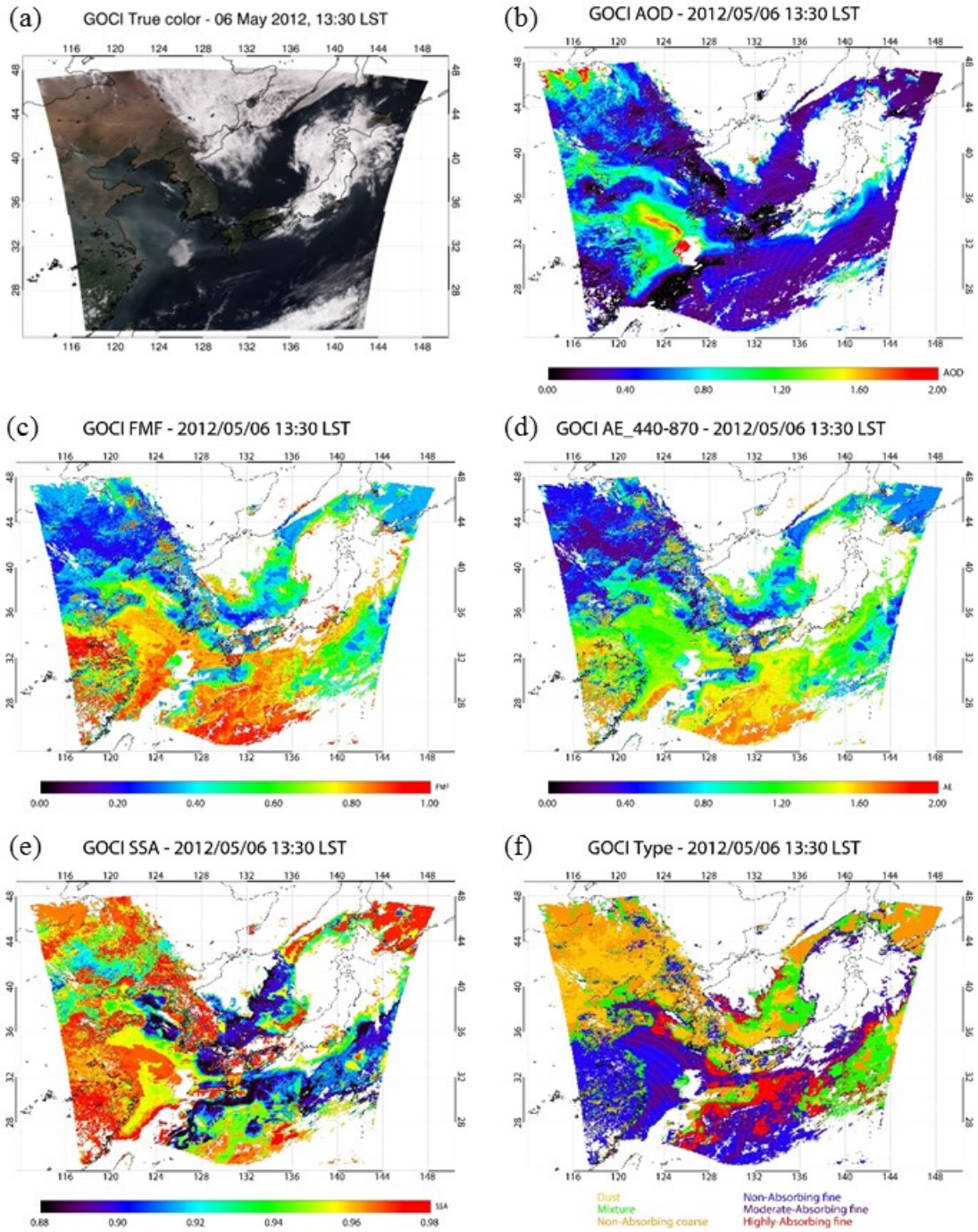

943

944 Figure 6. Images of (a) GOCI true color, (b) AOD at 550 nm, (c) FMF at 550 nm, (d) AE
945 between 440 and 870 nm, (e) SSA at 440 nm, and (f) type for 6 May 2012, 13:30 LST.
946 Aerosol types are colored yellow (Dust), green (Mixture), orange (Non-absorbing coarse

type), blue (Non-absorbing fine type), purple (Moderately absorbing fine type), and red (Highly absorbing fine type).

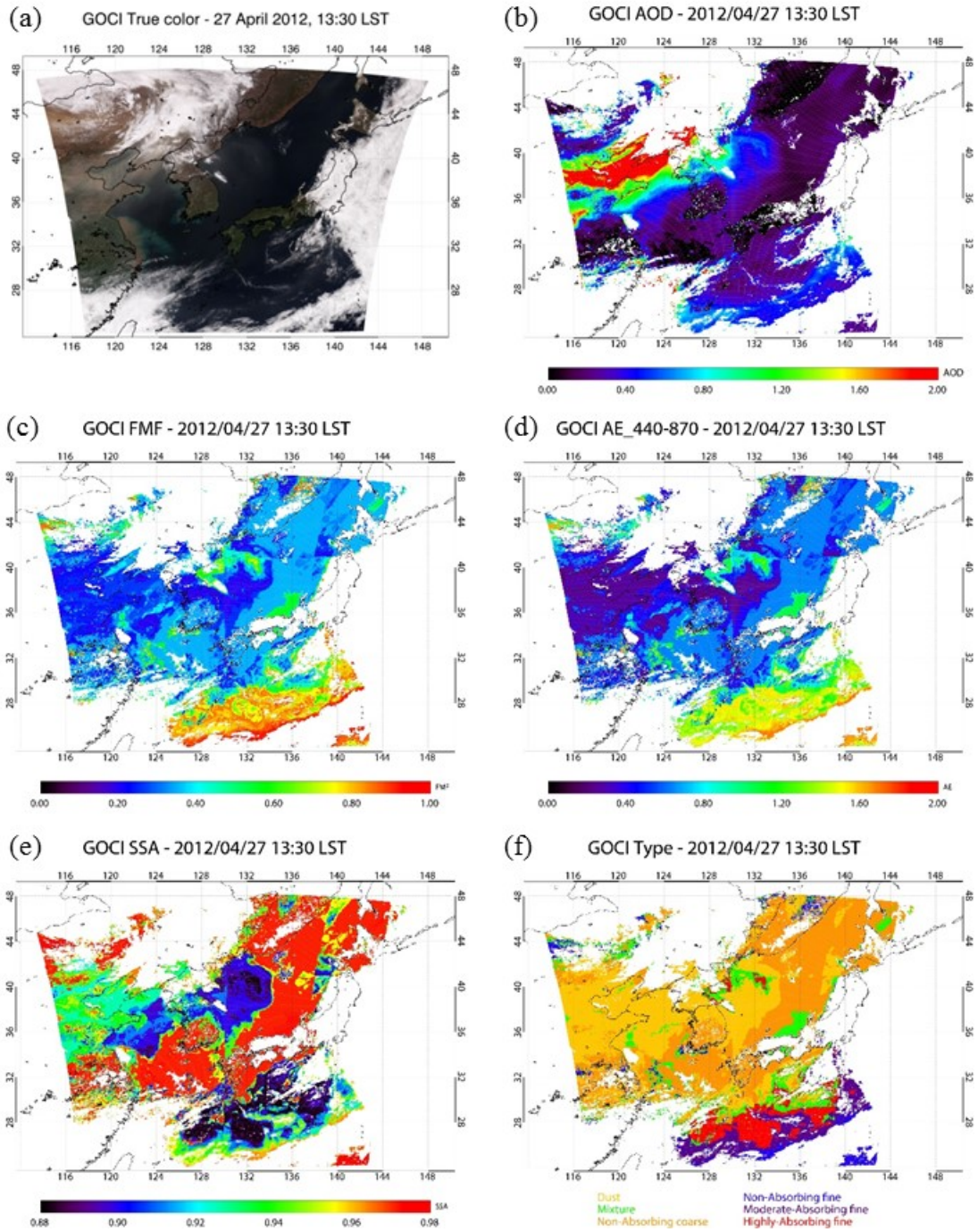

951

952 Figure 7. As Figure 6 except for 27 April 2012.

953

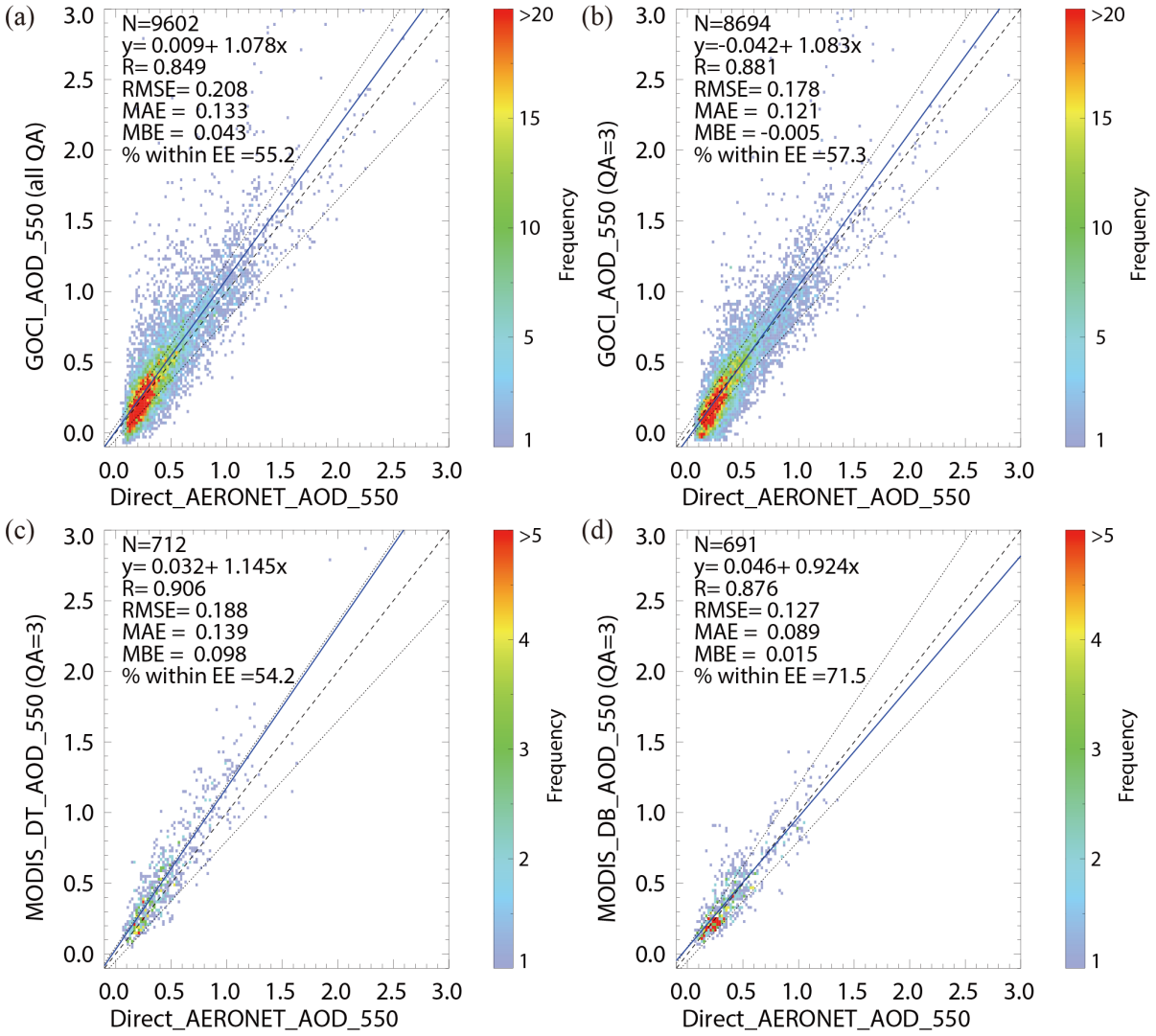

954

955 Figure 8. Comparison of AOD between AERONET and (a) GOCI for all QA, (b) GOCI for
956 QA = 3 only, (c) MODIS DT, and (d) MODIS DB. Colored pixels represent a bin size of 0.02.
957 The blue solid line is the linear regression line. Black dashed and dotted lines are the one-to-
958 one and expected error lines, respectively.

959

960

961 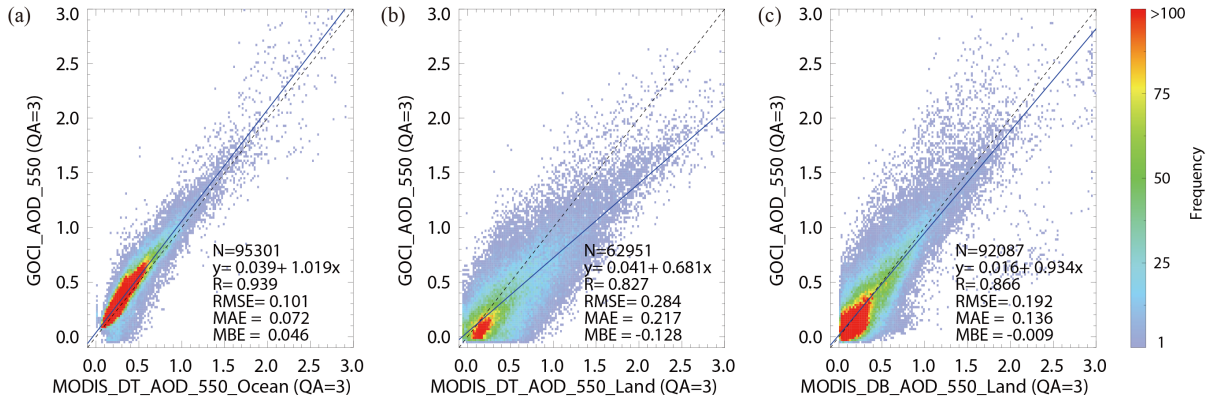

962 Figure 9. Comparison of AOD between (a) MODIS DT and GOCI over ocean, (b) MODIS
963 DT and GOCI over land, and (c) MODIS DB and GOCI over land. Color pixels represent a
964 bin size of 0.02. The blue solid line is the linear regression line. The black dashed line is the
965 one-to-one line.

966

967

968 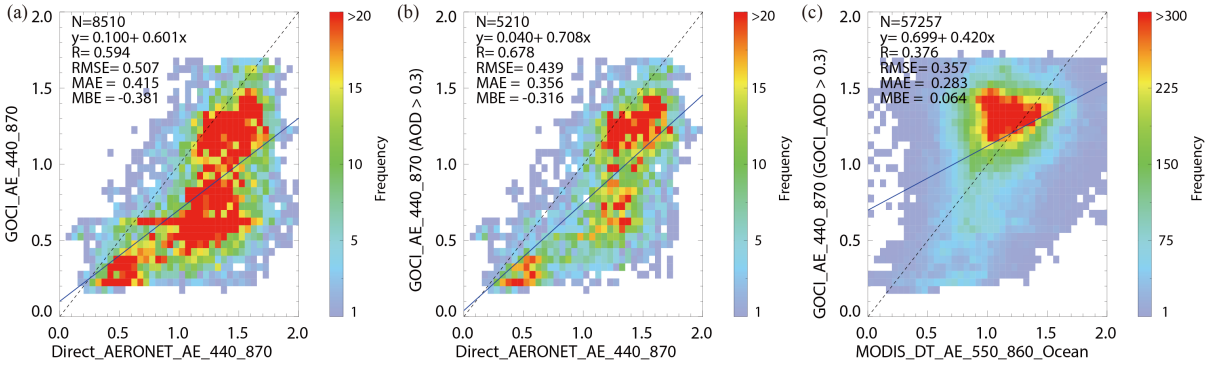

969 Figure 10. Comparison of AE between direct AERONET and GOCI for (a) all AERONET
970 AOD range, and (b) only for AERONET AOD > 0.3. (c) AE inter-comparison between
971 MODIS DT and GOCI over ocean only for GOCI AOD > 0.3. Colored pixels represent a bin
972 size of 0.05. Wavelengths of Angstrom exponents are 440 and 870 nm for AERONET and
973 GOCI, and 550 and 860 nm for MODIS DT over ocean. Dashed and solid lines are the same
974 as Figure 9.

975

976 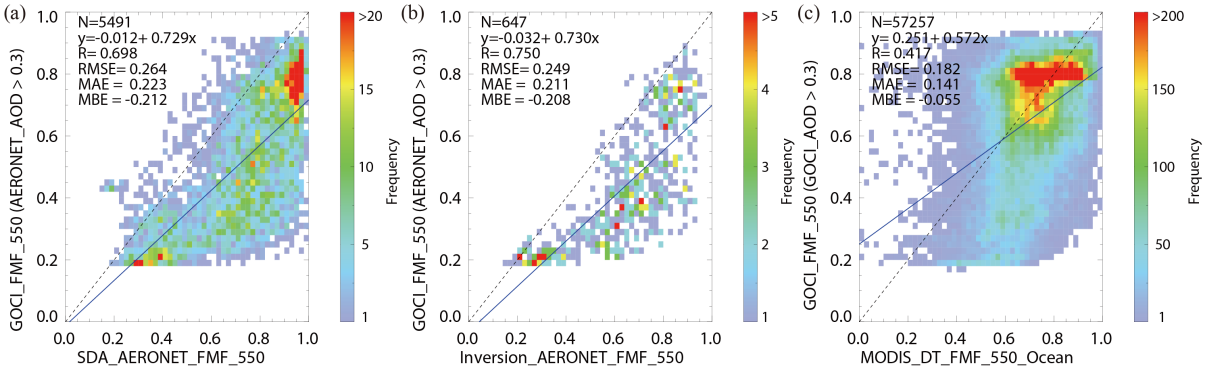

977 Figure 11. Comparison of FMF between (a) SDA AERONET and GOCI, and (b) inversion
978 AERONET and GOCI only for AERONET AOD > 0.3. (c) FMF inter-comparison between
979 MODIS DT and GOCI over ocean only for GOCI AOD > 0.3. Colored pixels represent a bin
980 size of 0.05. Dashed and solid lines are the same as Figure 9.

981

982

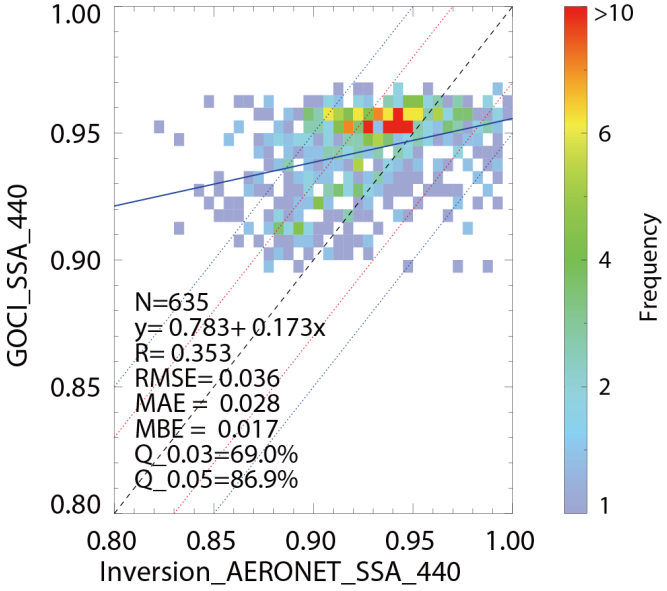

983

984 Figure 12. Comparison of SSA between inversion AERONET and GOCI. Colored pixels
985 represent a bin size of 0.005. Dashed and solid lines are the same as Figure 9. Red and blue
986 dotted lines are the ±0.03 and ±0.05 ranges, respectively.

987

988

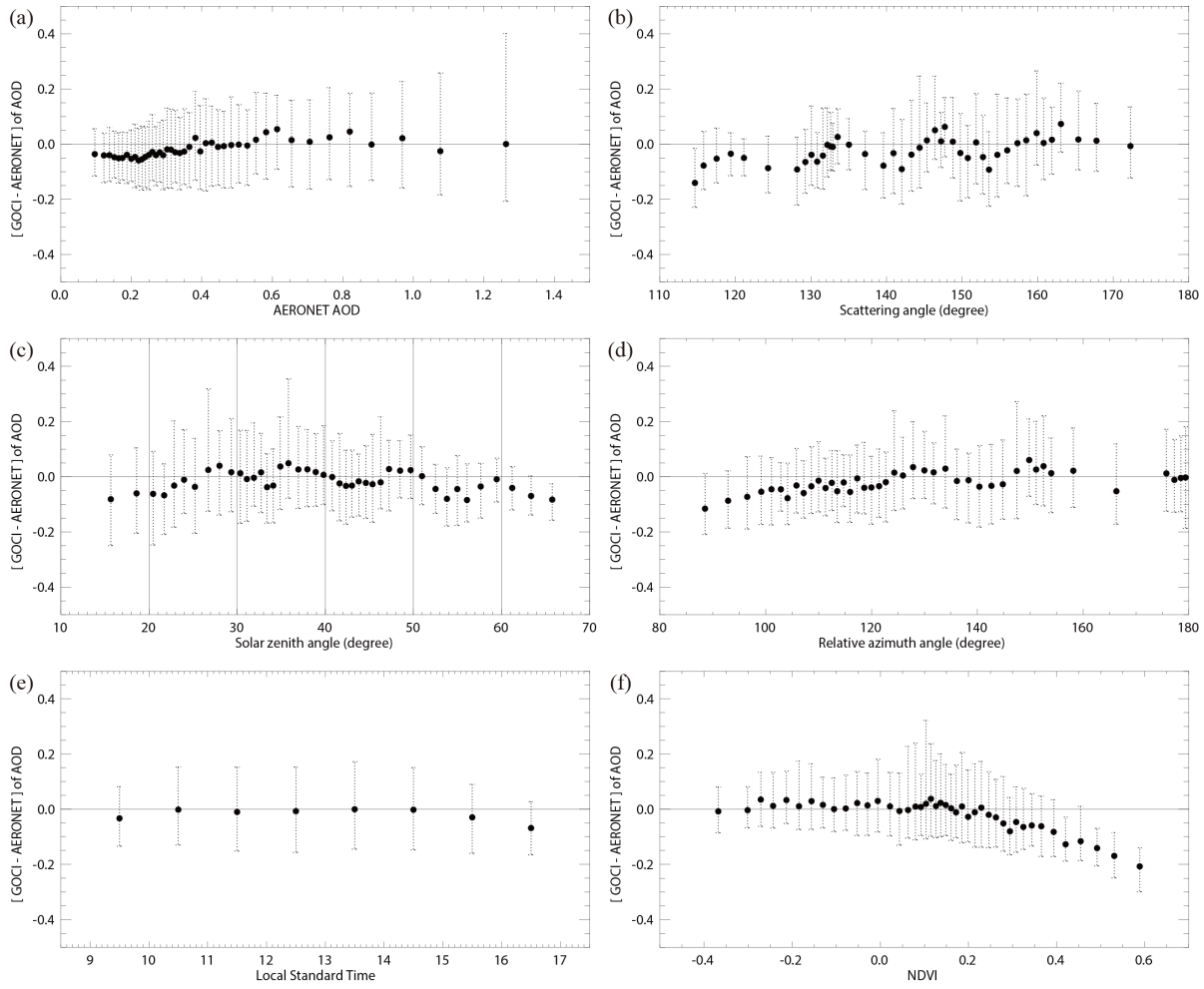

989

990 Figure 13. Difference in AOD between GOCI and AERONET according to (a) AERONET
991 AOD, (b) scattering angle, (c) solar zenith angle, (d) relative azimuth angle, (e) local standard
992 time, and (f) NDVI. Each point is the median value from 200 collocated data sorted in
993 ascending order of each x-axis value except for local standard time. Lower and upper bounds
994 of the error bar at each point correspond to the 16% and 84% points of each bin, respectively
995 (1 sigma interval).

996

997